Thermoacoustic stabilization of a longitudinal combustor using adjoint methods.

José G. Aguilar* and Matthew P. Juniper†

Engineering Department, University of Cambridge, Cambridge CB2 1PZ, United Kingdom

(Dated: July 7, 2020)

We construct a low order thermoacoustic network model that contains the most influential physical mechanisms of a thermoacoustic system. We apply it to a laboratory-scale longitudinal combustor that has been found to be thermoacoustically unstable in experiments. We model the flame, which is behind a bluff body, by a geometric level set method. We obtain the thermoacoustic eigenvalues of this configuration and examine a configuration in which six eigenmodes are unstable. We then derive the adjoint equations of this model and use the corresponding adjoint eigenmodes to obtain the sensitivities of the unstable eigenvalues to modifications of the model geometry. These sensitivities contain contributions from changes to the steady base flow and changes to the fluctuating flow. We find that these two contributions have similar magnitudes, showing that both contributions need to be considered. We then wrap these sensitivities within a gradient-based optimization algorithm and stabilize all six eigenvalues by changing the geometry. The required geometry changes are well approximated by the first step in the optimization process, showing that this sensitivity information is useful even before it is embedded within an optimization algorithm. We examine the acoustic energy balance during the optimization process and identify the physical mechanisms through which the algorithm is stabilizing the combustor. The algorithm works by, for each mode, reducing the work done by the flame, while simultaneously increasing the work done by the system on the outlet boundary. We find that only small geometry changes are required in order to stabilize every mode. The network model used in this study deliberately has the same structure as one used in the gas turbine industry in order to ease its implementation in practice.

I. INTRODUCTION

Thermoacoustic oscillations are a major challenge for rocket and gas turbine designers. In gas turbines they frequently appear in designs for lean premixed combustion (which reduces NO_x emissions) or fuel flexibility (which reduces reliance on fossil fuels) [1]. These oscillations increase heat transfer to the chamber walls, create noise, and can cause structural damage, all of which are undesirable.

There are several ways to mitigate or eliminate thermoacoustic instabilities. The addition of a passive device, such as a Helmholtz resonator, is a relatively simple way to dampen a specific oscillation [2]. However, with a few exceptions (see e.g., [3, 4]), most of these devices can only dampen a narrow band of frequencies. The addition of active control has also proven to be effective in laboratory combustors and full scale rigs [5–7]. It adapts to changing operating conditions but depends critically on the effectiveness and durability of the sensors and actuators, and is not sufficiently safe for commercial use, particularly in aircraft.

In this paper we develop and apply a passive control approach that does not rely on Helmholtz resonators. The growth or decay rate of thermoacoustic oscillations is exceedingly sensitive to particular changes in the acoustic characteristics of a combustion chamber and the flame's behavior [8]. On the one hand, this explains why thermoacoustic oscillations are so difficult to eliminate through good design: even if a given design is stable, small subsequent changes can render it unstable. On the other hand, this opens up the possibility that all oscillations could be stabilized through small design changes, if a systematic way to discover these changes could be devised. An encouraging fact is that all operational gas turbines and rocket engines are thermoacoustically stable, even though this stability is sometimes reached only after a lengthy design process.

The sensitivity of eigenvalues (i.e., natural frequencies) of a thermoacoustic model can be obtained very cheaply using adjoint methods [9–12]. With adjoint methods, all the sensitivities of a given eigenvalue can be calculated for roughly the same computational cost as the original eigenvalue calculation [13]. (Tutorials on this with sample code can be found in Juniper and Sujith [8], Juniper [11].) These sensitivities can be combined in order to calculate how an eigenvalue is affected by any given change to the system geometry, boundary conditions, or flame behavior. With these it should be possible to derive small system changes that stabilize all unstable thermoacoustic oscillations. For example, in a simple case Magri and Juniper [9] stabilized a simple thermoacoustic model using a drag device and a secondary heat source. These findings were experimentally verified by Rigas *et al.* [14], Jamieson *et al.* [15]. For a

---

* Now at Norges teknisk-naturvitenskapelige universitet (NTNU); jose.aguilar@ntnu.no

† mpj1001@cam.ac.uk

Helmholtz resonator, Caeiro *et al.* [16] obtained a target impedance by performing adjoint-based shape optimization on its neck. For a 2D periodic combustor, Mensah and Moeck [17] tuned and positioned multiple acoustic dampers to stabilize thermoacoustic modes in a system that resembles an annular combustor. For an annular combustor, Yang *et al.* [18] found the position and geometry of Helmholtz resonators to ensure optimal acoustic damping.

In most of the studies mentioned above, the changes affect the unsteady flow but not the steady flow. In some thermoacoustic models, such as Helmholtz solvers, the steady flow is not included so an unsteady adjoint calculation such as that in Juniper [11] is sufficient. In other thermoacoustic models, such as the network model used in this paper, the steady flow can be included. If it is, the sensitivity of the eigenvalue to changes in the steady flow also needs to be calculated. For the hydrodynamic oscillation of the flow around a cylinder, Marquet *et al.* [19] showed that when a small control cylinder is placed downstream, the eigenvalue is five times more sensitive to the steady force from the cylinder than it is to the unsteady force. This shows that the sensitivity to changes in the steady flow is not necessarily small.

In this paper we calculate all the eigenvalues (natural frequencies) of a thermoacoustic system using a low order network model similar to one used in industry [20]. We identify the handful of unstable modes and use adjoint methods to calculate the sensitivities of their growth rates with respect to geometric parameters such as the areas, lengths and mean radii of the ducts in the network. We include their influence on the flame transfer function. We input these sensitivities into an optimization routine which seeks to simultaneously stabilize all modes, while also ensuring that other modes do not become unstable. The result is a configuration that is stable to all thermoacoustic modes. Finally we examine the sources and sinks of acoustic energy over a cycle in order to identify the physical mechanisms that the optimization routine employs to stabilize all modes in the system simultaneously. This stabilization procedure is performed on several modes at a single operating condition. In a practical device, all the thermoacoustic modes must be stable at the steady-state operating points (e.g. take-off, cruise, and idle for an aircraft engine). It would be straightforward to extend the technique developed in this paper to several operating points.

II. GOVERNING EQUATIONS OF THE NETWORK MODEL

Due to their versatility, accuracy, and speed, low-order network models are widely used both in industry and academia. Examples include LOTAN [21], OSCILOS [22] and TA3 [23]. See Lieuwen [24] for a detailed introduction to the methods and Bothien [25, Chapter 4] for a review of network models currently in use. The low order network model used in this paper is based on the model originally developed in Stow and Dowling [26, 27, 28], and is described in detail in Aguilar [29]. It is governed by the Euler equations:

$$\frac{\partial \rho}{\partial t} + \nabla \cdot (\rho \boldsymbol{u}) = 0, \tag{1a}$$

$$\rho \frac{\partial \boldsymbol{u}}{\partial t} + \rho (\boldsymbol{u} \cdot \nabla) \boldsymbol{u} + \nabla p = \boldsymbol{f}, \tag{1b}$$

$$\frac{\partial p}{\partial t} + \boldsymbol{u} \cdot \nabla p + \gamma p \nabla \cdot \boldsymbol{u} = (\gamma - 1) Q, \tag{1c}$$

where ρ is the density, $\boldsymbol{u}$ is the velocity vector, p is the pressure, γ is the ratio of specific heat capacities, $\boldsymbol{f}$ is a body force, and Q is the rate of heat release. In this paper we use the one dimensional form of the equations and, following the formalism developed in Stow and Dowling [26], we linearize around a steady uniform base flow. The flow variables take the form $p = \bar{p}(x) + p'(x,t)$. Further, a modal decomposition with complex frequency ω is performed such that the perturbations become $p'(x,t) = \text{Re}\{\hat{p}(x)e^{i\omega t}\}$. The acoustic network is then divided into three types of modules: straight ducts, connecting ducts and boundaries, as described below.

A. Straight ducts

The main network elements are the straight ducts characterized by length, L, mean radius, R, and area, A. In these ducts, the governing equations for the steady base flow are:

$$\bar{\rho}\frac{\mathrm{d}\bar{u}}{\mathrm{d}x} + \bar{u}\frac{\mathrm{d}\bar{\rho}}{\mathrm{d}x} = 0, \qquad \bar{\rho}\bar{u}\frac{\mathrm{d}\bar{u}}{\mathrm{d}x} + \frac{\mathrm{d}\bar{p}}{\mathrm{d}x} = 0, \qquad \bar{u}\frac{\mathrm{d}\bar{p}}{\mathrm{d}x} + \bar{\gamma}\bar{p}\frac{\mathrm{d}\bar{u}}{\mathrm{d}x} = 0, \tag{2}$$

which imply that the base flow in a given duct is constant and homogeneous. The governing equations for fluctuating flow are:

$$i\omega\hat{\rho} + \bar{\rho}\frac{\mathrm{d}\hat{u}}{\mathrm{d}x} + \bar{u}\frac{\mathrm{d}\hat{\rho}}{\mathrm{d}x} = 0, \qquad i\omega\bar{\rho}\hat{u} + \bar{\rho}\bar{u}\frac{\mathrm{d}\hat{u}}{\mathrm{d}x} + \frac{\mathrm{d}\hat{p}}{\mathrm{d}x} = 0, \qquad i\omega\hat{p} + \bar{u}\frac{\mathrm{d}\hat{p}}{\mathrm{d}x} + \bar{\gamma}\bar{p}\frac{\mathrm{d}\hat{u}}{\mathrm{d}x} = 0. \tag{3}$$

Quantity	Steady base flow	Fluctuating flow
Mass flux (m)	$\bar{m} = A\bar{\rho}\bar{u}$	$\hat{m} = A(\bar{\rho}\hat{u} + \hat{\rho}\bar{u})$
Momentum flux (f_x)	$\bar{f}_x = A(\bar{p} + \bar{\rho}\bar{u}^2)$	$\hat{f}_x = A(\hat{p} + \hat{\rho}\bar{u}^2 + 2\bar{\rho}\bar{u}\hat{u})$
Energy flux (e)	$\bar{e} = \bar{m}\left(\bar{h} + \frac{1}{2}\bar{u}^2\right)$	$\hat{e} = A\left(\frac{\bar{\gamma}\bar{u}}{\bar{\gamma}-1}\hat{p} + \bar{\rho}\left(\bar{h} + \frac{3}{2}\bar{u}^2\right)\hat{u} + \bar{u}\left(\bar{h} - \frac{\bar{\gamma}\bar{p}}{(\bar{\gamma}-1)\bar{\rho}} + \frac{1}{2}\bar{u}^2\right)\hat{\rho}\right)$
Entropy (s)	$\bar{s} = \bar{s}^o - R_g\ln(\bar{p})$	$\hat{s} = \bar{c}_v\left(\frac{\hat{p}}{\bar{p}} - \bar{\gamma}\frac{\hat{\rho}}{\bar{\rho}}\right)$

TABLE I: Mean and fluctuating components for fluxes and entropy.

These equations can be decomposed into three travelling waves: one convective wave (A_E) that propagates with velocity $\bar{u}$ and two acoustic waves that propagate upstream (A_-) and downstream (A_+) with velocities $\bar{c} \pm \bar{u}$, where $\bar{c} = \sqrt{\bar{\gamma}\bar{p}/\bar{\rho}}$ is the speed of sound. The corresponding mode shapes are given by:

$$\hat{p}(x) = A_+\mathrm{e}^{ik_+x} + A_-\mathrm{e}^{ik_-x}, \quad \hat{\rho}(x) = \frac{1}{\bar{c}^2}\left(A_+\mathrm{e}^{ik_+x} + A_-\mathrm{e}^{ik_-x} - A_E\mathrm{e}^{ik_0x}\right), \quad \hat{u}(x) = \frac{1}{\bar{\rho}\bar{c}}\left(A_+\mathrm{e}^{ik_+x} - A_-\mathrm{e}^{ik_-x}\right), \quad (4)$$

where the wavenumbers, defined using the Mach number $\bar{M} = \bar{u}/\bar{c}$, are:

$$k_\pm = \frac{\omega}{\bar{c}}\left(\frac{\bar{M}\mp 1}{1 - \bar{M}^2}\right), \qquad\qquad k_0 = \frac{\omega}{\bar{u}}. \qquad (5)$$

At the joints between ducts, fluxes are conserved, such as mass flux $m = A\rho u$, momentum flux $f_x = Ap + mu$, energy flux $e = m(h + \frac{1}{2}u^2)$, and in some cases entropy $s = s^o - R_g\ln(p)$. Here $h = \int c_p(T)\,\mathrm{d}T$ is the enthalpy and $s^o = \int c_p(T)/T\,\mathrm{d}T$ is the entropy function, which varies only with temperature. $c_p(T)$ is the specific heat capacity at constant pressure, R_g is the ideal gas constant and $c_v(T) = c_p(T) - R_g$ is the specific heat capacity at constant volume. Finally, the temperature $T = p/(\rho R_g)$ is defined by p and ρ through the ideal gas law. This flux formulation is valid for semi-perfect gases, as described in [30]. The mean and fluctuating quantities of the fluxes are given in table I. Further details on the conversion between wave amplitudes, flow perturbations and flux perturbations, as well as wave propagation inside the ducts, can be found in Stow and Dowling [26].

B. Connecting modules

The modules used to connect ducts are modelled using conservation of fluxes in a control volume which is assumed to be compact – i.e. the length of the control volume is much shorter than the acoustic wavelength. For simplicity we will consider the fluxes in vector form such that $\boldsymbol{f_i} = [m_i, f_{x_i}, e_i]^T$ and $\boldsymbol{s_i} = [m_i, s_i, e_i]^T$ where the subindex $i = 1$ represents the position upstream and $i = 2$ represents the position downstream of the control volume. For longitudinal configurations the relevant connecting modules are:

- **Area increase**: a sudden expansion, which is non-isentropic. This requires conservation of mass and energy fluxes. The axial momentum flux is increased by the force on the sides of the control surface approximated by the product between the upstream pressure and the difference in areas.

$$\boldsymbol{f_2} = \boldsymbol{f_1} + [0\,,\ p_1(A_2 - A_1)\,,\ 0\,]^T \qquad (6a)$$

- **Area decrease**: a sudden contraction, which is isentropic. Mass and energy fluxes are conserved.

$$\boldsymbol{s_2} = \boldsymbol{s_1}. \qquad (6b)$$

- **Heat source**: a region of heat addition into the system. Mass and momentum fluxes are conserved. The energy flux is increased by the rate of heat release Q:

$$\boldsymbol{f_2} = \boldsymbol{f_1} + [0\,,\ 0\,,\ Q]^T. \qquad (6c)$$

For this module the steady rate of heat release is given by $\bar{Q} = \eta \bar{m}_1 h_r$, where η is the efficiency and h_r is the enthalpy of reaction. The unsteady rate of heat release is assumed to be given by:

$$\frac{\hat{Q}}{\bar{Q}} = \text{FTF}(\omega, \bar{u}, A_k, R_k, L_k)\frac{\hat{u}_1}{\bar{u}_1}, \tag{7}$$

where FTF is the flame transfer function, which is a function of the mean velocity, the frequency and the geometric parameters A_k, R_k and L_k as shown in §III A.

C.   Boundary conditions

We assume that the inlet is located at $x = 0$, and the outlet at $x = L_t$ and consider:

- **Inlet boundary condition**: this is modelled with an acoustic reflection coefficient R_{ci} that assumes no entropy waves ($A_E = 0$) and is given as the ratio between reflected (A_+) and incident (A_-) acoustic waves:

$$A_+ - R_{ci}A_- = 0. \tag{8}$$

In this paper R_{ci} is treated as a constant complex number.

- **Outlet boundary condition**: this is modelled with another reflection coefficient R_{co} defined in a similar way to the inlet reflection coefficient:

$$A_- \mathrm{e}^{ik_- L_t} - R_{co}A_+ \mathrm{e}^{ik_+ L_t} = 0. \tag{9}$$

D.   Nonlinear eigenvalue problem

Using the modules described above we build a network model that resembles a combustor. To obtain the eigenvalues we first solve the steady equations for the steady base flow. Then, using a shooting method, we form the dispersion relation from which the eigenvalues are computed. We begin with an initial guess for ω and propagate from the inlet boundary condition, through each module, to the outlet boundary condition. Usually this boundary condition will not be satisfied so we update the value of ω and iterate until the outlet boundary condition is satisfied. The value of $\omega = 2\pi f - i\lambda$ is then an eigenvalue of the system, with frequency f and growth rate λ. The associated global mode is given by $\{\omega; \hat{\rho}, \hat{u}, \hat{p}\}$.

III.   LINEAR STABILITY ANALYSIS OF A LONGITUDINAL COMBUSTOR

A.   Model description

The thermoacoustic system considered in this paper is a 10 kW longitudinal combustor built in Cambridge University Engineering Department, originally intended for the experimental investigation of the response of turbulent premixed flames to acoustic oscillations [31]. One of the experimental cases focuses on a configuration with no swirl and imperfectly premixed combustion and is prone to self-excited oscillations. The geometry consists of an inlet duct connected to a plenum with a varying cross section at both ends. This is followed by the neck which contains the fuel injection plane and a centred bluff body used to stabilize the flame. The outlet is a cylindrical pipe which contains the flame. The configuration is shown in Fig. 1.

To model this rig we consider a total of 124 straight ducts. The conical cross sections either side of the plenum are modelled as a sequence of 50 area increases and 50 area decreases. A convergence analysis on the eigenvalues shows that, to capture the frequency accurately, the conical sections can be modelled by single abrupt junctions. To capture the growth rates accurately, however, at least 10 steps are required. For this model we use 50 steps to ensure that the conical sections are well represented. The bluff body at the entrance to the combustion chamber is modelled as a sequence of 20 area decreases. We consider the working fluid to be a semi-perfect gas with the properties of air, as given in McBride *et al.* [32]. The inlet temperature is 300 K. We assume that air is supplied at a constant mass flow rate of $\bar{m} = 5.516 \times 10^{-3}$ kg/s to match the experimental measurement at the bluff body of $\bar{u} = 9.90$ m/s [31]. We consider an open outlet at atmospheric pressure and a flame anchored to the bluff body. To match the experimental results and LES simulations [33] we model the steady heat input with a combustion efficiency of $\eta = 0.90$, fuel properties of ethylene, and an equivalence ratio of $\phi = 0.61$.
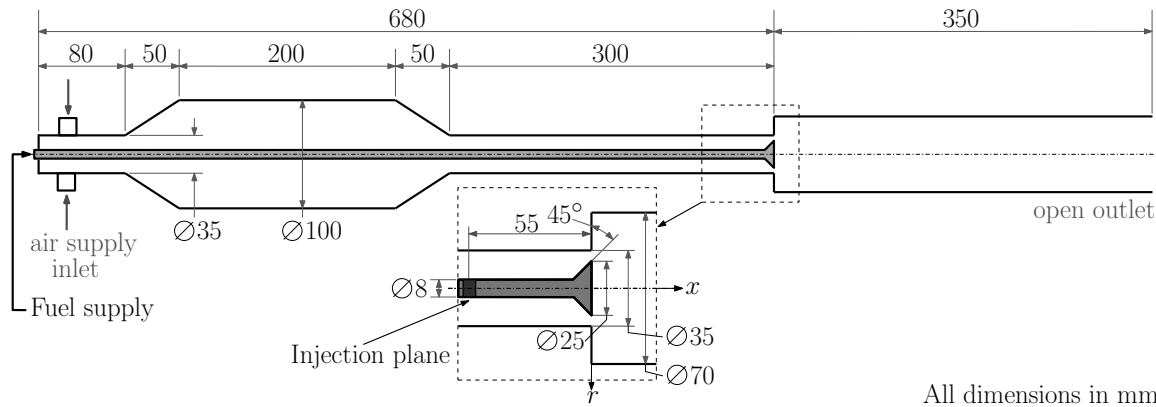
FIG. 1: Schematic of the longitudinal combustor. Air and fuel enter on the left and are mixed between a fuel injection plane and a bluff body combustor. A short flame sits just downstream of the bluff body combustor.

For the boundary conditions we consider an inlet modelled by an acoustic reflection coefficient with $R_{ci} = 0.85 + 0.10i$, which resembles the impedance of an almost-closed end. The outlet is modelled with the frequency-dependent reflection coefficient of a circular duct radiating sound originally proposed by Levine and Schwinger [34]. This model was extended to consider a mean flow in Cargill [35], Peters et $al.$ [36]. Taking r as the duct radius the reflection coefficient is given by:

$$R_{co} = -\left(1 + 0.9\frac{\bar{u}}{\bar{c}}\right)\left(1 - \frac{1}{2}\left(\frac{\omega r}{\bar{c}}\right)^2\right)e^{i(k_+ - k_-)0.6133r}. \tag{10}$$

The flame transfer function (FTF) used in this model is detailed in appendix A and shown in Fig. 2b. It depends on the geometric parameters that define the bluff body described above. It assumes a flow field inclined at an angle $\theta = \frac{1}{2}(\alpha + \beta)$. The angle $\alpha = 45°$ is computed from the network model using the difference between the inner radii of the last two ducts that compose the bluff body, together with the last duct's length (see Fig. 2a). A similar argument is used to define the angle β, which for this configuration is kept at $90°$. Furthermore, the FTF depends on a time delay given by $\tau = L_{inj}/\bar{u}$, with $L_{inj} = 55$ mm. Due to the presence of the area contraction at the bluff body the flow accelerates. This makes the time delay dependent on the base flow of several ducts. In order to eliminate this dependency we use instead an effective length $L_{eff} = 103$ mm, which is the equivalent length that the flow would have to travel at the constant velocity at the dump plane (9.9 m/s).

B. Stability Analysis

To perform the stability analysis we start from a set of initial guesses of the frequency between 0 and 1000 Hz. The solutions of the dispersion relation, which are eigenvalues of the system are shown in Fig. 3 overlaid on the logarithmic boundary condition error. The system shows that there are six unstable eigenvalues at 314, 371, 432, 566, 627 and 754 Hz. The second eigenvalue has a frequency which is close to the reported one (348 Hz in Balachandran [31]) at which the self-excited oscillations saturate. The accuracy of this modelling approach depends mainly on the characterization of the FTF and the boundary conditions. Using a similar network model and an FTF obtained from LES, Han et $al.$ [33] accurately computed the frequency at which the limit cycle saturates. The stable modes with growth rates around -30 s^{-1} appear due to the entropy wave at the outlet and are spaced approximately every 2 Hz. The pressure mode shapes of the 3 most unstable eigenvalues are shown in Fig. 4. For the modes at 371 and 566 Hz, the largest pressure fluctuations occur at the neck, while at 627 Hz the largest pressure fluctuations occur at the inlet and the neck.

IV. EIGENVALUE SENSITIVITY TO GEOMETRIC MODIFICATIONS

In order to stabilize this configuration, we need to know how each eigenvalue changes when the geometry changes. Consider, for example, a small increase, δA, in the area of one of the ducts. This causes a change in the steady base

(a) Flame fronts and geometric
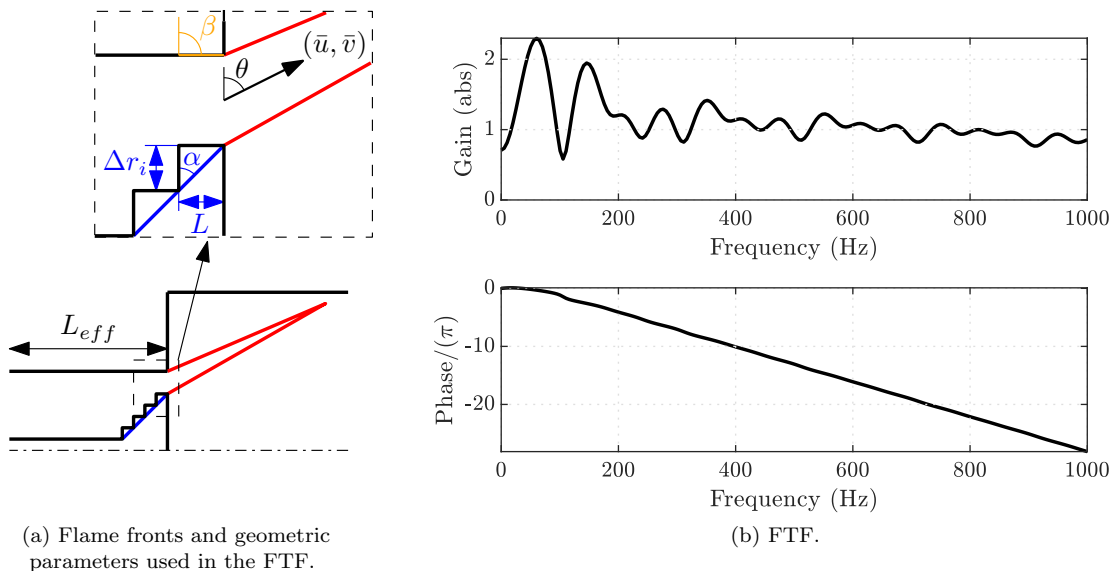parameters used in the FTF.

(b) FTF.

FIG. 2: (a) Geometry of the flame model. The flame fronts are drawn in red, the conical bluff body in blue, and the network model in black. In the network model, the bluff body is modelled as a series of ducts with decreasing area. The angle of the flow between the flame sheets is determined by the last two ducts. (b) The flame transfer function (FTF), which is derived from this flame geometry (see appendix A).
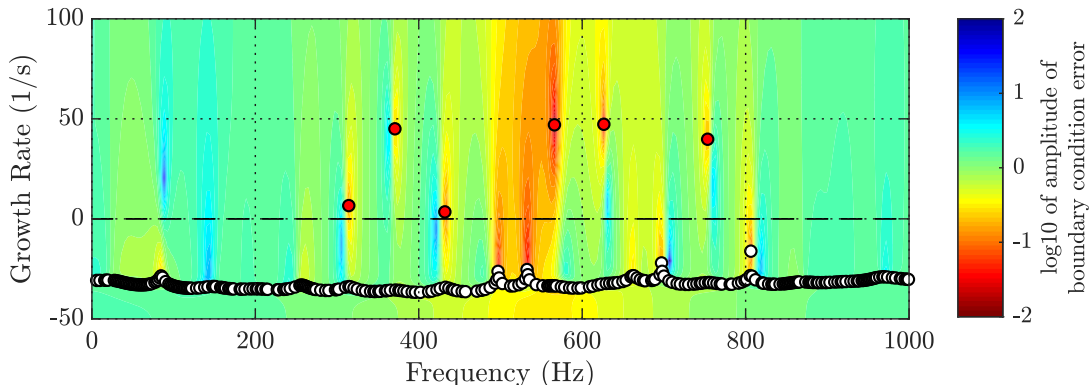

FIG. 3: The log of the error in the downstream boundary condition when a shooting method is applied from the upstream boundary of the network model. This is strongly negative for eigenvalues of the network model. The red markers show the six unstable eigenvalues (growth rate > 0). The white markers show the many stable eigenvalues.

flow and in the fluctuating flow (see Eqs. (6)). Each of these shifts the eigenvalue. The shift is given by:

$$\delta\omega = \left(\frac{\partial\omega}{\partial A_B} + \frac{\partial\omega}{\partial A_P} \right) \delta A. \tag{11}$$

In this context $\partial\omega/\partial A_B$ is the sensitivity of the eigenvalue to the changes in the base flow, and $\partial\omega/\partial A_P$ is the sensitivity due to the changes induced by the fluctuating flow. Each sensitivity can be separated into a frequency sensitivity and a growth rate sensitivity:

$$\frac{\partial\omega}{\partial A} = 2\pi\frac{\partial f}{\partial A} - i\frac{\partial\lambda}{\partial A}. \tag{12}$$

The sensitivities of the eigenvalue to each geometric parameter are derived using a Lagrangian formulation [37]. In this approach, the adjoint or co-state equations are derived first. Then the sensitivities are obtained by solving the optimality conditions. The geometric parameters considered in this paper can induce modifications in both the base flow and the fluctuating flow. Therefore two different sets of adjoint equations are required (see for example Marquet
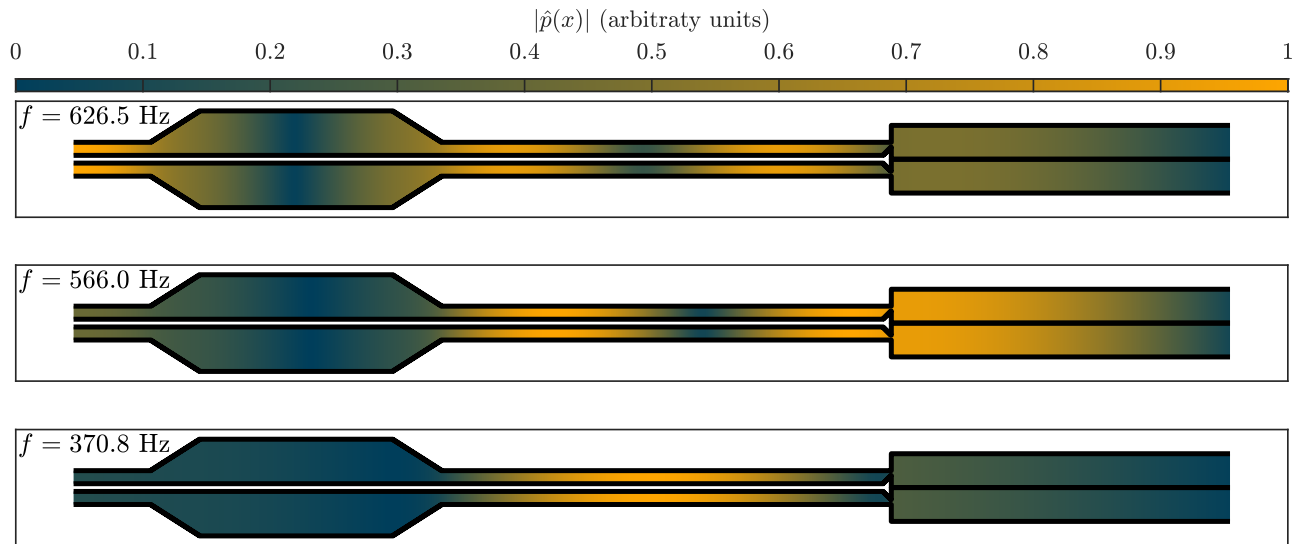
FIG. 4: Modulus of the pressure fluctuations of the 3 most unstable eigenvalues.

et al. [19]). These, together with the optimality conditions, are derived in appendix B. Further details can be found in Aguilar *et al.* [10], Aguilar [29]. The first set of adjoint equations corresponds to the adjoint eigenproblem of the fluctuating flow, which inputs the steady base flow and outputs the adjoint global modes. The adjoint global modes are used to compute the sensitivity of the eigenvalue to modifications in the fluctuating flow $\partial\omega/\partial A_P$. The second set of adjoint equations corresponds to the adjoint base flow, which inputs the base flow and the global modes of the direct and adjoint eigenproblems and outputs the adjoint base flow variables. The adjoint base flow variables are used to compute the sensitivity of the eigenvalue to modifications in the steady base flow $\partial\omega/\partial A_B$. This term, often neglected in thermoacoustic analyses, can be as large as the first one.

As shown in §III B, the system has six unstable eigenvalues, each of which has a different sensitivity to a given
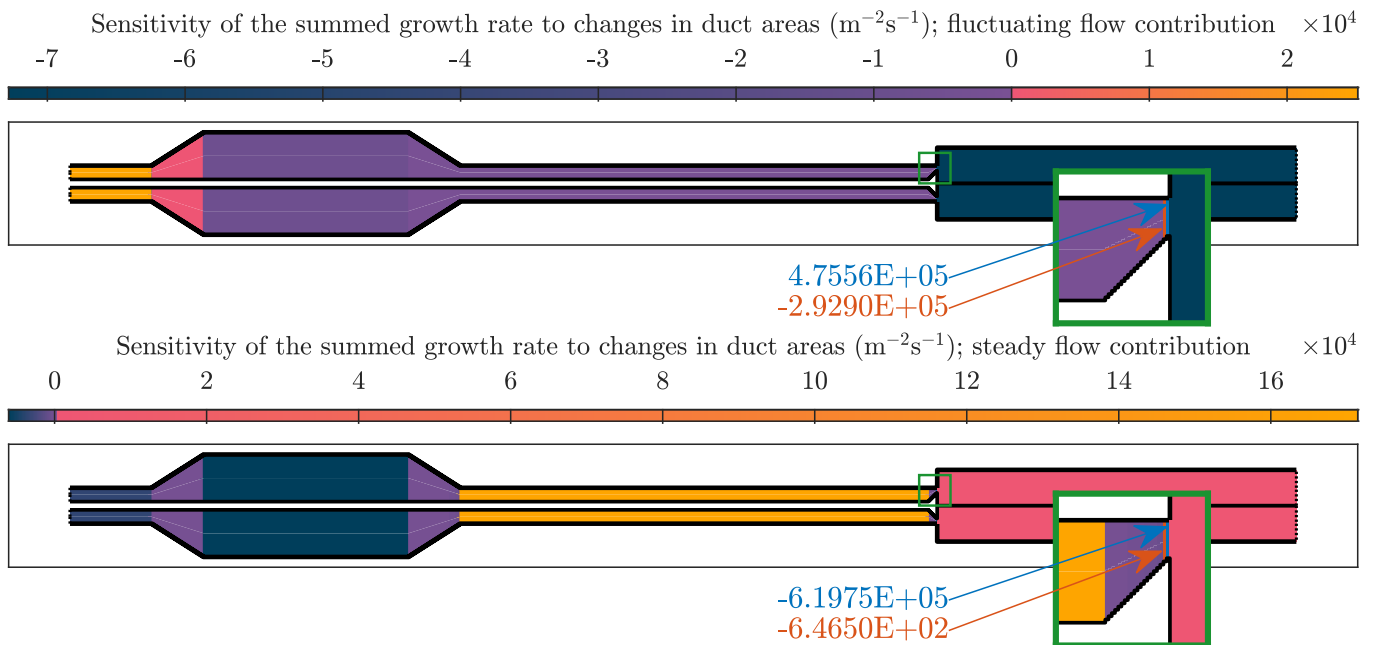

FIG. 5: The sensitivity of the growth rate (summed over the six unstable modes) to changes in duct areas. The top figure is the contribution from changes to the fluctuating flow. The bottom figure is the contribution from changes to the steady flow. The sensitivity to the final two ducts of the bluff body, which both affect the FTF (Fig. 2a), are indicated by blue and orange arrows in the inset figure.
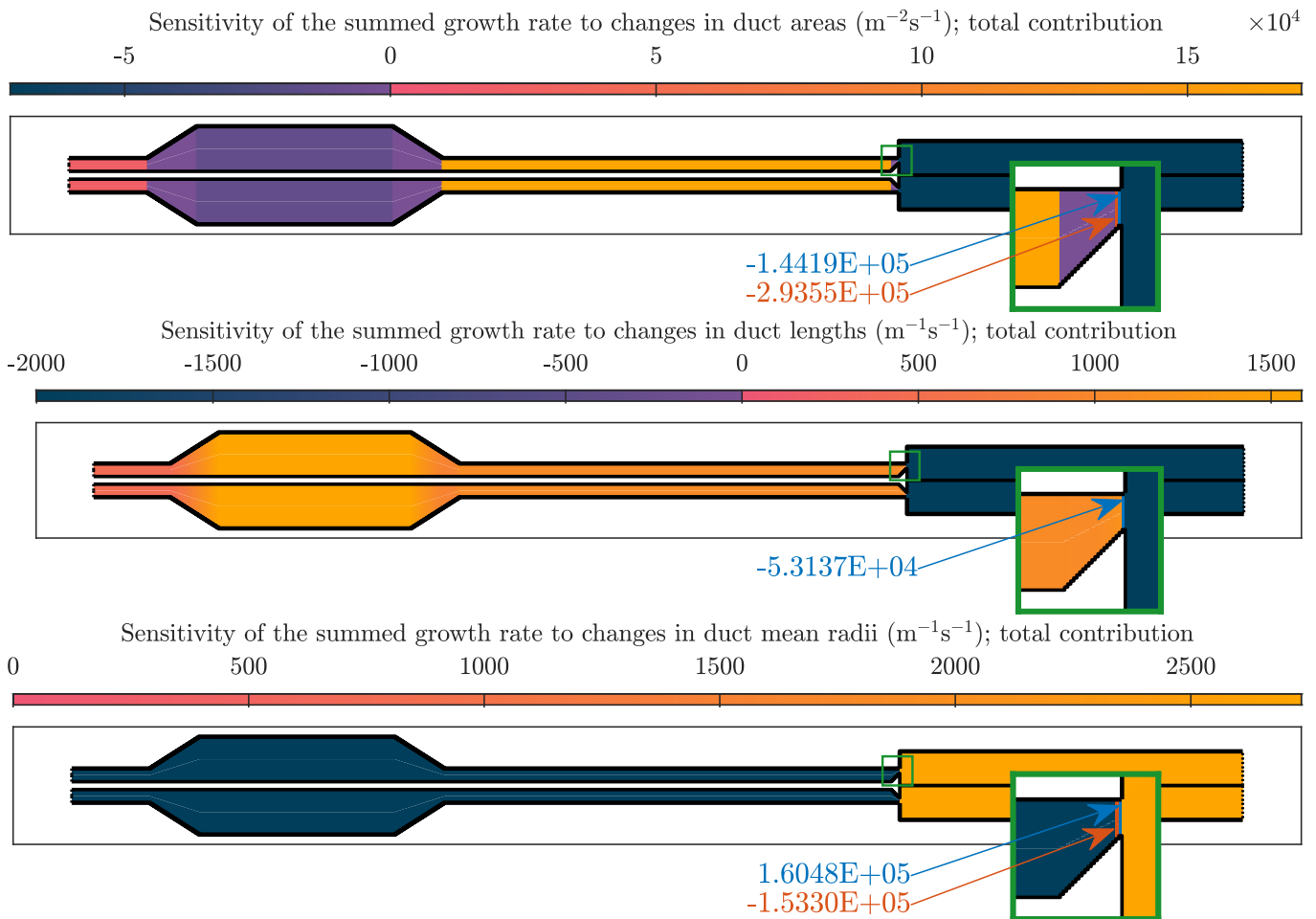
FIG. 6: The sensitivity of the growth rate (summed over the six unstable modes) to changes in duct areas (top), duct lengths (middle), and duct mean radii (bottom). The figures show the sum of the fluctuating flow and steady flow contributions. The sensitivity to the final two ducts of the bluff body, which both affect the FTF (Fig. 2a), are indicated by blue and orange arrows in the inset figure.

geometric change. For the optimization procedure we require a single cost function and, in this paper, we sum the growth rates of the unstable modes. The sensitivity of this cost function is shown in Fig. 5 for modifications acting through the fluctuating flow (top) and those acting through the steady flow (bottom). From this figure we observe that the sensitivities due to the fluctuating flow and steady flow have similar orders of magnitude, although in many regions they act in opposite directions. Furthermore, with the exception of the areas used to define the FTF, the regions with a large magnitude in one type of sensitivity have small magnitudes in the other type of sensitivity. In summary, the growth rate is sensitive to all geometry changes and there is no systematic trend. This confirms that thermoacoustic oscillations are sensitive to small design changes and reveals why a human designer, using intuitive design rules, would struggle to exploit them.

Next we calculate the sensitivity of the cost function (the sum of the unstable growth rates) to changes in areas, lengths, and mean radii, as shown in Fig. 6. The first observation is that the sensitivity to the last two ducts, which define the bluff body shape, are an order of magnitude larger than those due to the rest of the geometry. This is because they affect the FTF and the thermoacoustic system is particularly sensitive to the FTF. The area and length sensitivities of these ducts are negative, which implies that an increase in these parameters will be stabilizing. The second observation is that, with the exception of these two ducts, the length and mean radius sensitivities are two orders of magnitude smaller than the area sensitivities. This is because a change in area causes a change in the base flow, while a change in the length or mean radius does not. The second most influential factor is the area of the neck. From Fig. 6 we can estimate the changes required to stabilize the burner. These are: an increase in the angle of the bluff body as given by α in Fig. 2a; a reduction in the neck area and an increase of the combustion chamber area; shortening of the plenum's length; and an enlargement of the combustion chamber.

V.   STABILIZATION WITH AN OPTIMIZATION ROUTINE

The sensitivity analysis in the previous section provides gradient information that can be used in a gradient descent optimization algorithm. In this section we define a cost function, describe an optimization routine, and show the results from this combination.

A.   Cost function, constraints and parameters

We wish to converge to a system in which all eigenvalues decay in time and therefore set an objective growth rate λ_o to be negative for all eigenvalues. Then, if N_ω is the number of eigenvalues that have growth rates larger than λ_o and if $\boldsymbol{X}$ is the vector containing all the geometric parameters that define the combustor, i.e., $\boldsymbol{X} = [r_{o_1}, r_{o_2}, ..., r_{i_1}, ..., L_1, ...]^T$, then our cost function is:

$$\mathcal{J}(\boldsymbol{X}) = \frac{1}{2} \sum_{j=1}^{N_\omega} \left(\lambda_j(\boldsymbol{X}) - \lambda_o \right)^2 . \tag{13}$$

This is a measure of the total distance between the targeted eigenvalues and the objective growth rate. Notice that if an eigenvalue lies below λ_o it is not included in the cost function. This means that if, during an iteration, a stable mode becomes unstable, the cost function will not take that contribution into account until the following iteration.

In order to minimize the cost function we use a conjugate gradient method [38] in which the gradient of $\mathcal{J}$ is computed from the adjoint-based sensitivities. Performance is increased if all the parameters have similar magnitudes. Here, rather than rescaling the parameters, we simply use the inner radii r_i, outer radii r_o and lengths L instead of the areas A, mean radii R and lengths L. In each iteration, once the descent direction has been computed, the length of the step is set to be the negative of the gradient. This can be very large (because eigenvalues are often very sensitive to geometry changes) so we also ensure that the parameters do not change by more than a given percentage (denoted ΔX_m), which is enforced with a backtracking procedure. Further details about the implementation can be found in Aguilar [29].

The conical sections of the plenum and bluff body are modelled by 50 or 20 short straight ducts. Instead of allowing each of these ducts to change individually, we constrain the section to remain conical. The radii and lengths of these ducts are therefore determined just by the inlet radius, outlet radius, and length of the conical section. Fig. 7 shows these conical sections (blue), the geometric parameters that are allowed to change (black), and the geometric parameters that are fixed (in red). The fixed parameters are: the mass flow rate at the inlet; the inner radius representing the fuel line r_{i_1}, in order to avoid variations in the fuel supply; the effective length from injection to the base of the flame; the outlet pressure.
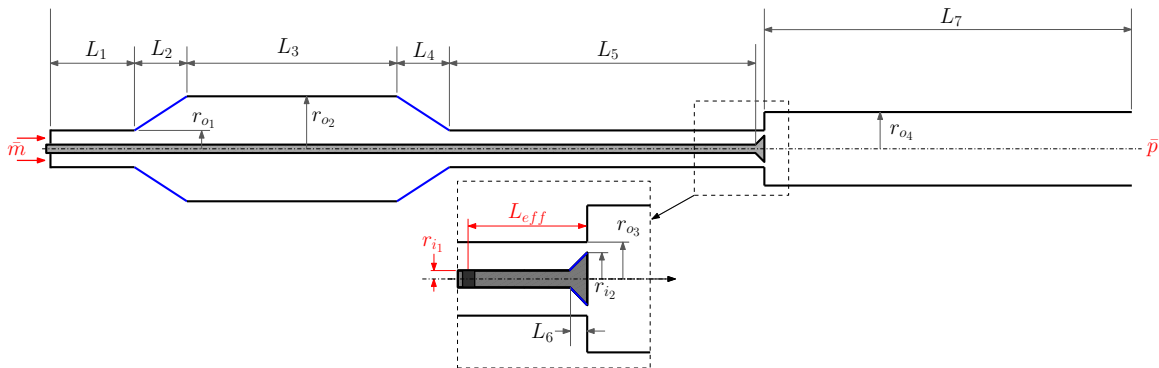

FIG. 7: Geometric parameters used in the optimization routine. The parameters in black are allowed to be updated. The parameters in red are kept constant. The blue lines denote regions that are constrained by adjacent parameters.

B.   Optimization routine

For the optimization routine we use an objective growth rate of $\lambda_o = -5\ \mathrm{s}^{-1}$. The routine can work with quite large step sizes but, in order to show the trajectories of the eigenvalues as they are stabilized (Fig. 9), we constrain the

Inlet	Area increase	Plenum	Area decrease	Neck	Bluff body	Combustion chamber
$\tilde{r}_{o_1} = -0.0316$	–	$\tilde{r}_{o_2} = 0.0134$	–	$\tilde{r}_{o_3} = -0.2151$	–	$\tilde{r}_{o_4} = 0.1070$
$\tilde{r}_{i_1} = 0.0000$	–	–	–	–	$\tilde{r}_{i_2} = -0.2237$	–
$\tilde{L}_1 = -0.0007$	$\tilde{L}_2 = -0.0034$	$\tilde{L}_3 = -0.0015$	$\tilde{L}_4 = -0.0045$	$\tilde{L}_5 = -0.0005$	$\tilde{L}_6 = 0.2093$	$\tilde{L}_7 = 0.0010$

TABLE II: Relative changes of the geometric parameters that define the longitudinal combustor for the case with $\Delta X_m = 0.1\%$.

maximum parameter change to be $\Delta X_m = 0.1\%$ and $\Delta X_m = 0.5\%$. We stop the algorithm when the cost function becomes smaller than 0.02.

For a given shift in growth rate, longer wavelength oscillations require larger geometric changes than shorter wavelength oscillations. We therefore start by stabilizing the low frequency (i.e., long wavelength) oscillations. First we stabilize all the modes below 500 Hz, without regard to the remaining modes. We do this with a local cost function $\mathcal{J}_L(\boldsymbol{X})$. Then we include all the modes up to 1000 Hz with a total cost function $\mathcal{J}_T(\boldsymbol{X})$. The values of the cost functions at every iteration are shown in Fig. 8 and show straightforward behavior. The local cost function always decreases, while the global cost function oscillates when only part of the frequency range is being considered, and then reduces rapidly when the entire range is considered. By comparing the black and red lines, one can see that, as expected, the process requires fewer iterations if ΔX_m is bigger. The trajectories of the eigenvalues in the complex plane (Fig. 9) from their initial positions (red dots) to their final positions (white diamonds) also show straightforward behavior.

Fig. 10 compares the initial configuration (black) with the optimized configuration (red). As expected, due to the high sensitivity to the geometric parameters, all of the modes can be stabilized by small changes to the geometry. For a given parameter, X, we define the relative change as $\tilde{X} = X/X_0 - 1$, where the subindex 0 denotes the initial value. The relative change in the magnitude of the optimization parameters defined in Fig. 7 are shown in table II.

The most prominent changes are in the neck and the bluff body, which are the regions with highest sensitivity in the initial configuration. To stabilize the system, the neck reduces its radius by 22%. This modifies the mean flame front and therefore the FTF (Fig. 11). In detail, the neck reduction increases the bulk velocity in the dump plane, which decreases the flame time delay. However, it also increases the flame angle α to 61°, which lengthens the flame and increases the flame time delay. The former effect outweighs the latter and the time delay reduces, as seen by the shallower gradient of the phase line in Fig 11b. It is worth noting that most of the changes were correctly predicted by the single sensitivity analysis in §IV.
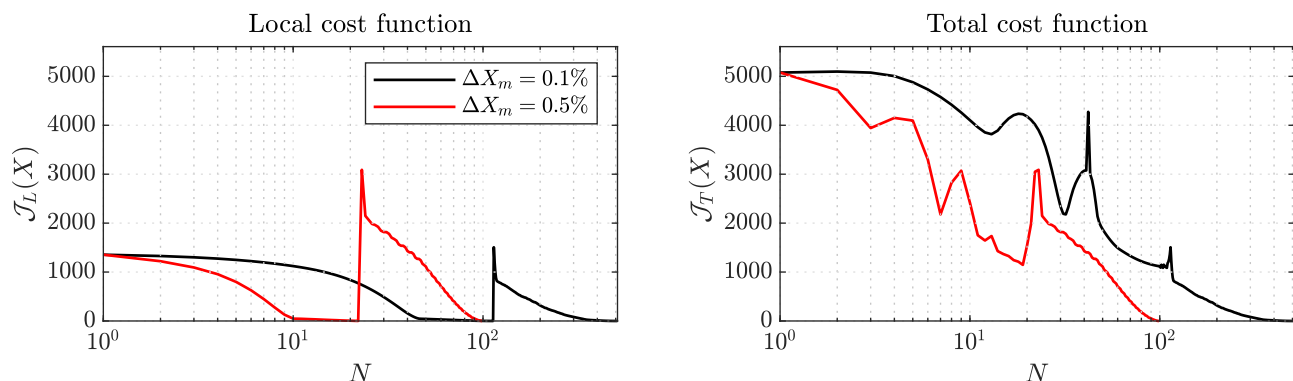

FIG. 8: Cost functions as a function of iteration, N, for small steps ($\Delta X_m = 0.1\%$) and large steps ($\Delta X_m = 0.1\%$). The left figure shows the local cost function ($\mathcal{J}_L$), which is that minimized in the optimization algorithm. This is initially the square of the sum of the growth rates of all the modes with frequencies below 500 Hz and subsequently (for $N > 22$ or $N > 120$) the square of the sum of the growth rates of all the modes below 1000 Hz. The right figure shows the total cost function ($\mathcal{J}_T$), which is the square of the sum of the growth rates of all the modes below 1000 Hz.
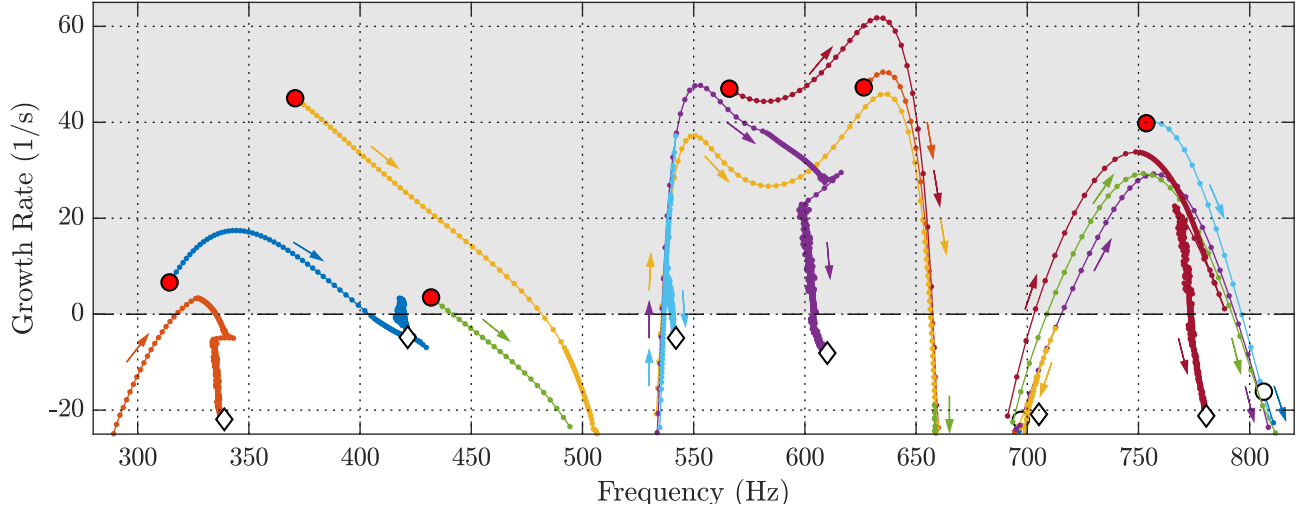
FIG. 9: Trajectories of the complex eigenvalues during the optimization process shown in Fig. 8 for $\Delta X_m = 0.1\%$. The round markers show the initial eigenvalues, colored red if unstable and white if stable. The white diamonds show the eigenvalues at the end of the optimization process, when they have all been stabilized.
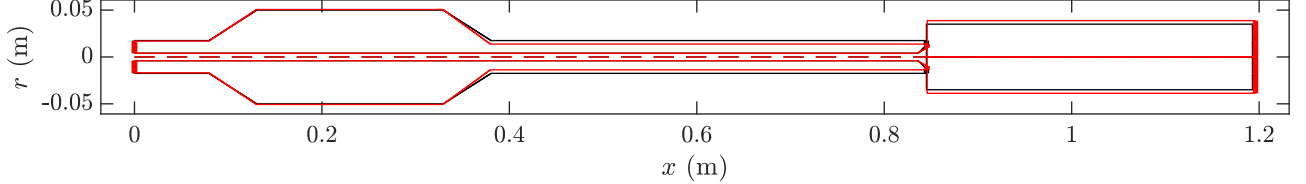

FIG. 10: Plot of the unstable initial (black) and stable final (red) configurations of the longitudinal combustor for the optimization process with $\Delta X_m = 0.1\%$.

(a) Initial (black) and final (red) flame fronts.

(b) Initial (black) and final (red) flame transfer functions.
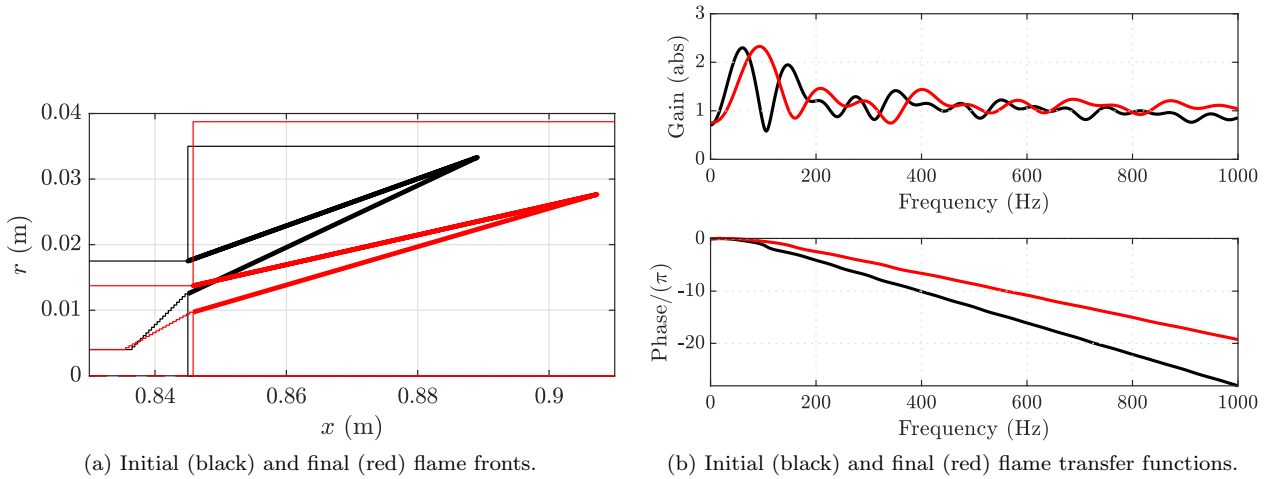
FIG. 11: Diagrams of the initial (black) and final (red) flame fronts and the initial (black) and final (red) flame transfer functions for the optimization process with $\Delta X_m = 0.1\%$.

VI. DISTURBANCE ENERGY BALANCE DURING THE OPTIMIZATION PROCESS

The optimization process works and, from a practical point of view, can be considered as a black box. Nevertheless, it is interesting to analyse the optimization process from a physical point of view in order to determine the mechanisms that are being exploited in order to stabilize all the eigenvalues. For this we calculate the balance of the disturbance energy over a cycle for all of the modes as they are stabilized. We begin by introducing the one dimensional disturbance

energy equation [39–41]:

$$\frac{\partial E}{\partial t} + \frac{\partial W}{\partial x} = D + D_n \tag{14}$$

where

$$E = \frac{1}{2}\frac{p'^2}{\bar{\rho}\bar{c}^2} + \frac{1}{2}\bar{\rho}u'^2 + \rho'\bar{u}u' + \frac{1}{2}\frac{\bar{\rho}\bar{T}s'^2}{\bar{c}_p}, \tag{15}$$

$$W = p'u' + p'\frac{\rho'}{\bar{\rho}}\bar{u} + \bar{\rho}\bar{u}u'^2 + \rho'\bar{u}^2u' + \frac{\bar{u}}{R_g}p's' - \bar{u}\bar{T}\rho's', \tag{16}$$

$$D = \frac{\bar{u}}{R_g}s'\frac{\partial p'}{\partial x} - \bar{u}\bar{T}s'\frac{\partial \rho'}{\partial x}, \tag{17}$$

$$D_n = \left(\bar{\rho}\bar{u}\left(\frac{T'}{\bar{T}}\right) - (\bar{\rho}u' + \rho'\bar{u})\right)s'\frac{\mathrm{d}\bar{T}}{\mathrm{d}x} - \frac{\bar{u}}{R_g\bar{p}}s'p'\frac{\mathrm{d}\bar{p}}{\mathrm{d}x} + \frac{\bar{u}\bar{T}}{\bar{\rho}}s'\rho'\frac{\mathrm{d}\bar{\rho}}{\mathrm{d}x} + q'\frac{T'}{\bar{T}} - \bar{q}\left(\frac{T'}{\bar{T}}\right)^2, \tag{18}$$

where q is the rate of heat release per unit volume. Here we separated D from D_n because, within each duct, the mean quantities are uniform ($\frac{\mathrm{d}[]}{\mathrm{d}x} = 0$) and $q' = \bar{q} = 0$. The terms in D_n are therefore zero. The contribution of the mean flow gradient and the heat sources enter the disturbance energy balance through the jump conditions between ducts, which will be considered below. We proceed by integrating Eq. (14) over the volume V_i of the ith duct and over the period of a given mode $\mathcal{T} = 1/f$. Using the divergence theorem we obtain:

$$\check{E}_i - \check{E}_{0_i} + \check{W}_{out_i} - \check{W}_{in_i} = \check{D}_i, \tag{19}$$

where

- the term $\check{E}_i - \check{E}_{0_i} \equiv \int_{V_i} E(t_0 + \mathcal{T}) - E(t_0)\,\mathrm{d}V_i$ is the change in energy in the ith duct over one cycle;

- the terms $\check{W}_{out_i} \equiv \int_{t_0}^{t_0+\mathcal{T}} A_i W_{out}\,\mathrm{d}t$ and $\check{W}_{in_i} \equiv \int_{t_0}^{t_0+\mathcal{T}} A_i W_{in}\,\mathrm{d}t$ correspond to the ratio of work done by the flow in the ith duct on its outlet and inlet boundaries respectively;

- the term $\check{D}_i \equiv \int_{t_0}^{t_0+\mathcal{T}} \int_{V_i} D\,\mathrm{d}V_i\,\mathrm{d}t$ corresponds to the fraction of energy of the ith duct generated or dissipated by convection of entropic disturbances.

Area changes and heat sources (i.e., jump conditions) correspond to regions where the mean flow quantities change. To compute their contribution to the disturbance energy balance we examine the terms that correspond to the ratio of work done by the flow on the boundaries of adjacent ducts. Consider, for example, a simple configuration with a flame that is located between two ducts. By summing Eq. (19) for $i = 1$ and $i = 2$, the corresponding energy balance for the system is given by:

$$\left(\check{E}_1 - \check{E}_{0_1}\right) + \left(\check{E}_2 - \check{E}_{0_2}\right) + \left(\check{W}_{out_1} - \check{W}_{in_1}\right) + \left(\check{W}_{out_2} - \check{W}_{in_2}\right) = \check{D}_1 + \check{D}_2. \tag{20}$$

After dividing by the total energy at the beginning of the cycle, the equation can be rewritten in physically descriptive terms as:

$$\check{E} - 1 = \check{W}_{outlet} - \check{W}_{inlet} + \check{W}_{flame} + \check{D}. \tag{21}$$

Here

- $\check{E} \equiv (\check{E}_1 + \check{E}_2)/\check{E}_{T_0}$ and $\check{D} \equiv (\check{D}_1 + \check{D}_2)/\check{E}_{T_0}$,

- $\check{E}_{T_0} \equiv \check{E}_{0_1} + \check{E}_{0_2}$, represents the total energy at the beginning of the cycle,

- $\check{W}_{outlet} \equiv -\check{W}_{out_2}/\check{E}_{T_0}$, represents the ratio of work done by the outlet boundary on the flow,

- $\check{W}_{inlet} \equiv -\check{W}_{in_1}/\check{E}_{T_0}$, represents the ratio of work done by the inlet boundary on the flow,

- $\check{W}_{flame} \equiv -(\check{W}_{out_1} - \check{W}_{in_2})/\check{E}_{T_0}$, represents the ratio of work done by the flame on the flow. This follows from the fact that the perturbation variables (ρ', u', p', s') in the integral of $\check{W}_{out_1}$ and $\check{W}_{in_2}$ can be expressed in terms of perturbation fluxes (m', f'_x, e'). Then, using the fluctuating part of Eq. (6c), specifically when substituting the energy jump condition $e'_2 = e'_1 + Q'$, the dependency of $\check{W}_{flame}$ on Q' becomes evident.

A similar approach can be performed for the area changes. Then for the studied configuration, Eq. (21) becomes:

$$\check{E} - 1 = \check{W}_{flame} + \check{W}_{outlet} - \check{W}_{inlet} + \check{W}_{ac} + \check{D}, \tag{22}$$

where $\check{W}_{ac}$ is the work done by all the area changes in the configuration.

In Figs. 12 and 13 we show the disturbance energy balance for the modes that start at 371 and 566 Hz respectively. Corresponding figures for the other modes are available in the supplementary materials. (In appendix C we show that the fraction of disturbance energy retained is exactly $\check{E} = \exp(2\lambda/f)$.) The contributions to the energy balance due to the changes in area and the inlet boundary are negligible compared to the rest of the terms and are omitted from the figures for clarity. At the start of the optimization routine, the modes are unstable and the energy growth, $\check{E} - 1$ (red line), is positive. The flame, $\check{W}_{flame} > 0$, acts as a strong source of disturbance energy, while the work done at the outlet boundary, $\check{W}_{outlet}$, and the convection of entropy disturbances, $\check{D}$, are weak sinks. The optimization algorithm renders both of these modes stable by greatly decreasing $\check{W}_{flame}$, while simultaneously slightly increasing the work done at the outlet boundary, $\check{W}_{outlet}$. The terms in $\check{D}$ are only relevant when there are entropy waves in the system. For our configuration the entropy waves are only prominent in the last duct (i.e., after the flame). The sign of the convection of entropy disturbances, $\check{D}$, is always opposite to that of $\check{E} - 1$. The energy balances for the other modes (supplementary materials) show the same behavior at the end of the optimization process when they all become stable.

For each mode the algorithm exploits the same physical mechanism to reduce $\check{W}_{flame}$. This is to make the heat release rate fluctuations occur in (or close to) quadrature with the temperature fluctuations. It achieves this for all modes simultaneously mainly by altering the FTF and slightly by altering the mode shapes. In other words, although the heat release rate from the flame remains as sensitive to acoustic perturbations as it was in the original configuration, the timing of the heat release rate is such that it does no more than a small amount of work on the acoustic modes, and this work is sufficiently small to be dissipated through the boundaries.
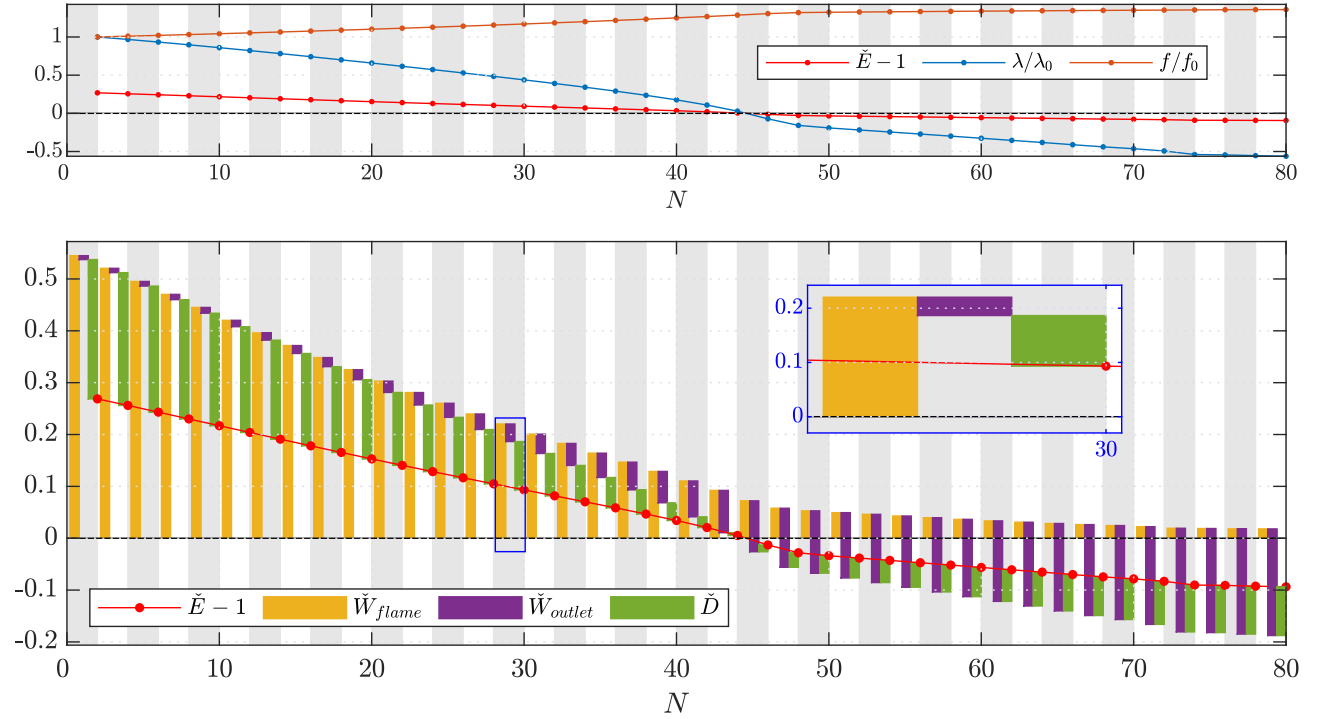

FIG. 12: Disturbance energy balance for the mode that starts at 371 Hz during the optimization process with $\Delta X_m = 0.1\%$. The top plot shows the disturbance energy growth (red), growth rate (blue), and frequency (orange) at each iteration. The growth rate and frequency have been normalized with respect to their initial values. The bottom plot shows the disturbance energy balance over one cycle Eq. (22) at each iteration. In this waterfall plot each iteration consists of three bar plots and a red line (see inset). The yellow bar shows the work done by the flame. The purple bar shows the work done at the outlet. The green bar shows the work done by the convection of entropic disturbances, which changes sign when the growth rate changes sign. The total disturbance energy growth over a cycle is the sum of these and is shown by the red round marker.
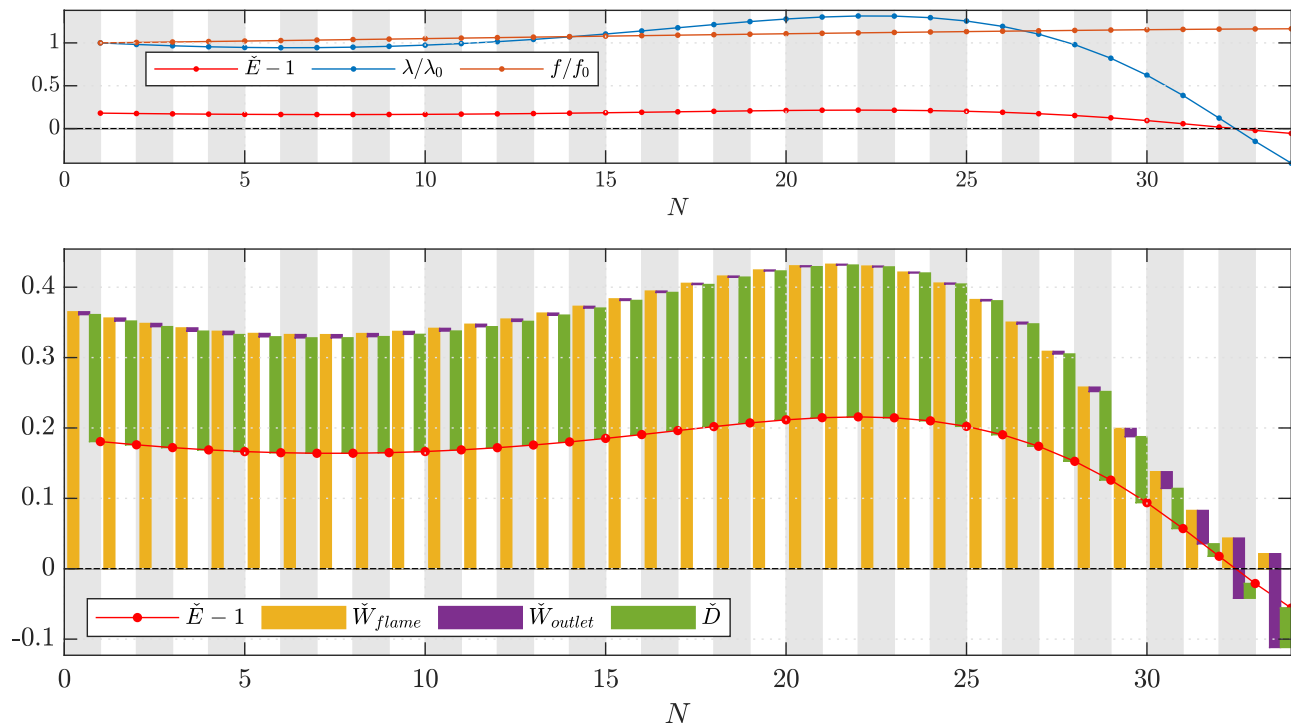
FIG. 13: As in Fig. 12 but for the mode starting at 566 Hz.

VII. DISCUSSION

At the end of §V we mention that the geometry changes obtained through the optimization routine are similar to those predicted by the initial sensitivity analysis. This is, however, not always the case. A counter-example can be found where we allow the lengths of all the elements except L_6 to vary while keeping all the radii constant (L_6 is the length of the bluff body shown in Fig. 7). As shown in Fig. 14, all the lengths need to be substantially altered in order to stabilize this combustor and these alterations are not in the directions indicated by the initial sensitivity from Fig. 6. The initial sensitivity is not sufficient in this case because the eigenvalues are not very sensitive to the lengths (with the exception of L_6). Large length changes are therefore required and, as these changes are implemented, the sensitivities evolve away from their initial values. On the other hand, the eigenvalues are very sensitive to parameters that affect the FTF, such as L_6 and the duct radii. The system can therefore be stabilized with only small changes to these parameters. The fact that the required geometry changes are small means that the sensitivities remain close to their initial values during the optimization process. This explains why the geometry changes obtained through the optimization routine are similar to those predicted by the initial sensitivity analysis.
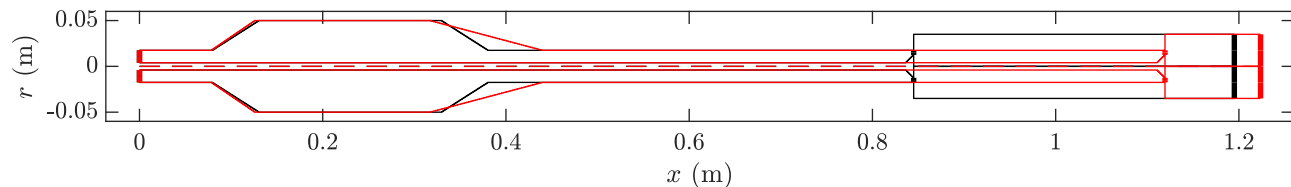

FIG. 14: Plot of the unstable initial (black) and stable final (red) configurations for the optimization routine where only the lengths are allowed to change, except for L_6.

Many stable designs, such as that in Fig. 14, can be achieved by modifying the cost function or the gradient descent algorithm. For simple burner geometries, such as the one used in this paper, gradient free algorithms can also be used, although these are more expensive than gradient descent algorithms. An example of a stable burner obtained using a genetic algorithm is shown in Fig. 15. This approach initializes the geometry at random within a given parameter space (for this problem the parameters were bounded to within 10% of their initial values). Therefore the method usually produces solutions that require larger changes than those obtained using adjoint methods. Given that

the adjoint methods are quicker and identify smaller geometry changes than gradient-free methods, they are likely to be preferred in practice. The most robust stable design can be found through uncertainty quantification on the eigenvalues [42] but this is out of the scope of this study.
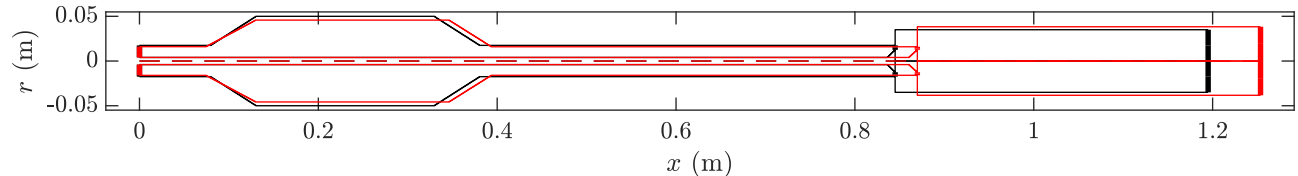

FIG. 15: Original unstable configuration (black) vs stable configuration (red) obtained using a genetic algorithm.

Finally we discuss two important scenarios, first when the method breaks and second the most unstable scenario. The method breaks when the algorithm is not allowed to change the most influential parameters. For example, if the bluff body, the neck radii, and the combustion chamber radii are fixed, the algorithm cannot change the FTF. It then changes the plenum radii and the lengths of all sections but becomes trapped in a local minimum in which some of the eigenvalues are still unstable. This result is shown in Fig. 16.
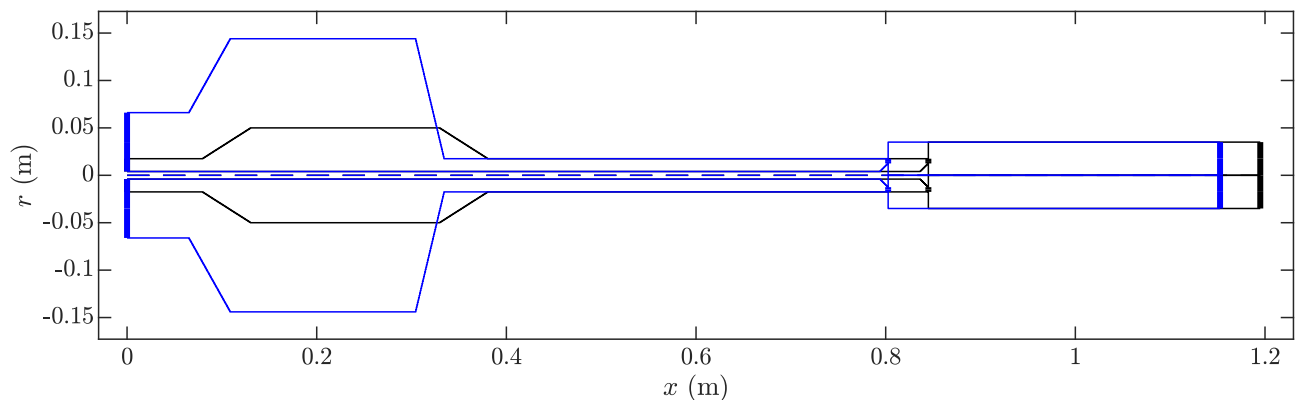

FIG. 16: Original unstable configuration (black) and unstable configuration (blue) obtained using the conjugate gradient algorithm, but without changing any of the parameters controlling the bluff body or combustion chamber.

On the other hand, it is interesting to see the most unstable configuration closest to our starting configuration. This scenario may be appropriate when trying to study self-excited cases in an otherwise stable combustor. To achieve this we change the objective growth rate to $\lambda_o = 200$ s^{-1} and use the same algorithm. We find that the most unstable configuration we can find, shown in Fig. 17, is only slightly more unstable than our starting configuration. This is because we had selected a particularly unstable starting configuration.

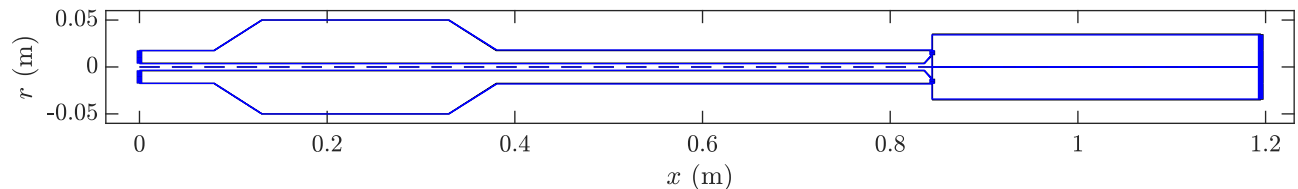FIG. 17: Original unstable configuration (black) and most unstable configuration (blue) obtained using the conjugate gradient algorithm setting $\lambda_o = 200$ s^{-1}.

VIII. CONCLUSIONS

In this paper we examine the thermoacoustic stability of a longitudinal combustor with several unstable modes. We perform eigenvalue sensitivity analysis using the adjoint equations in order to identify the sensitivity of all the

unstable modes to all the geometric parameters of the model. This process is computationally efficient because we use the adjoint equations, rather than a finite difference method. For the combustor in this paper we find that sensitivities due to changes in the base flow have similar magnitudes to sensitivities due to changes in the fluctuating flow. This shows that, as in hydrodynamic stability, the influence of base flow changes cannot necessarily be ignored in thermoacoustics. We also find that, as expected, the parameters that affect the flame transfer function (FTF) are particularly influential.

We then embed the adjoint-based gradient information inside an optimization algorithm in order to stabilize all of the modes in the combustor. The algorithm easily stabilizes all six modes with only small geometric changes. These geometric changes are the same as those that are predicted by considering a single calculation on the unstable configuration. This shows that design decisions based on eigenvalue sensitivity analysis are useful even before they are embedded within an optimization routine.

Tracking the balance of disturbance energy over a cycle reveals that the optimization process works by reducing the work done by the flame, while also increasing the work done through the downstream boundary. By the end of the routine it has achieved this for every mode. It is encouraging that, even for a configuration with six unstable modes, it is possible to find a similar configuration that has no unstable modes. This tallies with the observation that thermoacoustic instability has been eliminated from all operational gas turbines and rocket engines with small design changes, albeit sometimes after lengthy re-design.

The network model used in this paper deliberately mirrors that used by a large gas turbine manufacturer, so that it can be implemented in industry. The current study is for the longitudinal mode of a long thin combustor, and will be adapted next to azimuthal and longitudinal modes of an annular combustor. Industrial combustors have other constraints, such as lowering combustion emissions and being able to relight at high altitudes. These constraints, in the form of geometric constraints, can be embedded within the optimization algorithm described above. We have found that there are many possible stable configurations, so it is likely that a stable configuration can be attained even when other constraints are introduced.

Appendix A: Flame transfer function

The flame transfer function (FTF) used in this paper is the constant time delay FTF detailed in Xiaochuan Yuan *et al.* [43]. The FTF is obtained using the G-Equation (level set) method to track two flame fronts in a uniform flow, as shown in Fig. 2a. The only difference between the FTF shown in Xiaochuan Yuan *et al.* [43] and the one used in this paper is that we included the turbulent flame speed model by Lipatnikov and Chomiak [44]:

$$S_t = S_u \left(1 + 2.1 \left(\frac{u_t}{S_u} \right)^2 \right)^{\frac{1}{2}}, \tag{A1}$$

with turbulent velocity $u_t = 0.28$ m/s chosen in order to match the flame length as reported in Balachandran [31].

There are a few caveats in this modelling approach. First, a constant flow field inclined at an angle θ does not conserve mass on a cylindrical coordinate system. A better approach would be to use the potential flow described by a spherical source as in Graham [45], Semlitsch *et al.* [46]. In this paper we use the inclined flow model in order to retain an analytical FTF. Second, turbulent modelling of a flame front via the G-Equation requires the consideration of stochastic fluctuations [47], which are not considered in the proposed FTF. The derived FTF is laminar, and the turbuent flame speed is only included as a correction factor to match experimental results.

Appendix B: Adjoint equations and optimality conditions

In this appendix we derive the adjoint equations and optimality conditions for the network model. We begin by recasting the governing equations. First we consider $\boldsymbol{B}(G) = 0$ to be the vector of steady base flow equations, jump conditions and boundary conditions equated to zero, whose solution determines the base flow $G = \{\bar{u}, \bar{p}, \bar{\rho}, ...\}$ in the entire system. Next we consider $\boldsymbol{P}(\{\omega; \hat{\rho}, \hat{u}, \hat{p}\}, G) = 0$ to be the vector of fluctuating flow equations, jump conditions, and boundary conditions whose solution depends on the steady flow variables G and determines the global mode $\{\omega; \hat{\rho}, \hat{u}, \hat{p}\}$.

1.   Adjoint Equations

To obtain the continuous adjoint equations we create a Lagrangian functional. Considering $[\cdot, \cdot]$ as an appropriate inner product, the functional in its most general form is given by:

$$\mathcal{L} \equiv \omega - \left[\hat{q}^+, P(\{\omega; \hat{\rho}, \hat{u}, \hat{p}\}, G)\right] - \left[G^+, B(G)\right], \tag{B1}$$

where the eigenvalue ω is taken as the cost function, $\hat{q}^+$ is a vector of adjoint variables (Lagrange multipliers) associated with the fluctuating flow equations, G^+ is another vector of adjoint variables associated with the steady flow equations.

Ducts are governed by spatially varying functions, for example $a(x)$ and $b(x)$. Thus the corresponding inner product is given by:

$$\langle a(x), b(x) \rangle \equiv \int_{x_0}^{x_1} a(x)^* b(x) \; \mathrm{d}x, \tag{B2}$$

where * represents complex conjugation, and x_0 and x_1 represent the duct inlet and outlet positions. Jump conditions and boundary conditions are defined locally at positions x_0 or x_1 by single valued functions, for example c and d. Hence, the corresponding inner product is given by

$$\{c, d\} \equiv c^* d. \tag{B3}$$

To determine the sensitivity functions of the eigenvalue following a Lagrangian approach [37], any first variation of the Lagrangian with respect to a variable ξ must equate to 0, for any arbitrary perturbation $\delta\xi$:

$$\frac{\partial \mathcal{L}}{\partial \xi} \delta\xi \equiv \lim_{\epsilon \to 0} \left(\frac{\mathcal{L}(\xi + \epsilon\delta\xi) - \mathcal{L}(\xi)}{\epsilon} \right) = 0. \tag{B4}$$

For our problem there are four sets of variables of interest. Vanishing the derivatives of $\mathcal{L}$ in Eq. (B1) with respect to the:

1. **adjoint variables** (components of vectors $\hat{q}^+$ and G^+), corresponds to the trivial case since they return the already known perturbation $P(\{\omega; \hat{\rho}, \hat{u}, \hat{p}\}, G) = 0$ and base flow equations $B(G) = 0$;

2. **fluctuating variables** $(\hat{\rho}, \hat{u}, \hat{p})$, returns the adjoint fluctuating equations, used to compute the sensitivities of the eigenvalue to changes in the unsteady flow;

3. **base flow variables** G, returns the adjoint base flow equations, used to compute the sensitivities of the eigenvalue to changes in the steady base flow;

4. **eigenvalue** ω, returns the normalization condition.

2.   Adjoint fluctuating equations

To compute the adjoint fluctuating equations we examine the first inner product of the Lagrangian functional Eq. (B1).

a.   Straight ducts

For a straight duct, the relevant components of vector P in Eq. (B1) are given by Eqs. (3). Their corresponding adjoint variables (components of vector $\hat{q}^+$) are given by the spatial functions $[\hat{\rho}^+(x), \hat{u}^+(x), \hat{p}^+(x)]^T$ respectively. The resulting adjoint perturbation equations are:

$$i\omega^* \hat{\rho}^+ + \bar{u}\frac{\mathrm{d}\hat{\rho}^+}{\mathrm{d}x} = 0, \qquad i\omega^* \bar{\rho}\hat{u}^+ + \bar{\rho}\bar{u}\frac{\mathrm{d}\hat{u}^+}{\mathrm{d}x} + \bar{\rho}\frac{\mathrm{d}\hat{\rho}^+}{\mathrm{d}x} + \bar{\gamma}\bar{p}\frac{\mathrm{d}\hat{p}^+}{\mathrm{d}x} = 0, \qquad i\omega^* \hat{p}^+ + \bar{u}\frac{\mathrm{d}\hat{p}^+}{\mathrm{d}x} + \frac{\mathrm{d}\hat{u}^+}{\mathrm{d}x} = 0. \tag{B5}$$

The associated boundary terms are:

$$\left[\left(\hat{\rho}^{+*}\bar{u}\right)\delta\hat{\rho} + \left(\hat{\rho}^{+*}\bar{\rho} + \hat{u}^{+*}\bar{\rho}\bar{u} + \hat{p}^{+*}\bar{\gamma}\bar{p}\right)\delta\hat{u} + \left(\hat{u}^{+*} + \hat{p}^{+*}\bar{u}\right)\delta\hat{p} \right]_{x_0}^{x_1} = 0, \tag{B6}$$

where the δ symbol preceding the perturbation variables indicates that the boundary terms should vanish for any value of the perturbation variable. These terms are used to compute the jump conditions and to set the adjoint boundary conditions. Equations (B5) can be decoupled into two adjoint acoustic waves with amplitudes A_+^+ and A_-^+, which propagate downstream and upstream respectively, and one convective wave with amplitude A_E^+. The corresponding mode shapes are given by:

$$\hat{\rho}^+(x) = -\bar{c}^2 A_E^+ e^{ik_0 x}, \qquad \hat{p}^+(x) = A_+^+ e^{ik_+ x} + A_-^+ e^{ik_- x} + A_E^+ e^{ik_0 x}, \qquad \hat{u}^+(x) = \bar{c}\left(A_+^+ e^{ik_+ x} - A_-^+ e^{ik_- x}\right). \qquad (B7)$$

b.   Jump conditions

For jump conditions that are governed by the mass, momentum, and energy fluxes we define the following adjoint perturbation fluxes that depend on the side i of the jump condition:

$$\hat{\boldsymbol{f}}_{\boldsymbol{i}}^+ \equiv \begin{bmatrix} \hat{f}_{m_i}^+ \\ \hat{f}_{x_i}^+ \\ \hat{f}_{e_i}^+ \end{bmatrix} = \begin{bmatrix} \dfrac{1}{A_i}\left(\hat{\rho}_i^+ - \bar{u}_i \hat{u}_i^+ + \left(\dfrac{1}{2}(\bar{\gamma}_i-1)\bar{u}_i^2 + \bar{c}_i^2 - (\bar{\gamma}_i-1)\bar{h}_i\right)\hat{p}_i^+\right) \\ \dfrac{1}{A_i}\left(\hat{u}_i^+ - (\bar{\gamma}_i-1)\bar{u}_i \hat{p}_i^+\right) \\ \dfrac{1}{A_i}(\bar{\gamma}_i-1)\hat{p}_i^+ \end{bmatrix}. \qquad (B8)$$

Similarly, for jump conditions governed by mass and energy fluxes together with entropy conservation the following adjoint perturbation fluxes are defined:

$$\hat{\boldsymbol{s}}_{\boldsymbol{i}}^+ \equiv \begin{bmatrix} \hat{s}_{m_i}^+ \\ \hat{s}_{s_i}^+ \\ \hat{s}_{e_i}^+ \end{bmatrix} = \begin{bmatrix} \dfrac{1}{A_i}\left(\hat{\rho}_i^+ - \left(\dfrac{1}{2}\bar{u}_i + \dfrac{\bar{h}_i}{\bar{u}_i}\right)\hat{u}_i^+ + \bar{c}_i^2 \hat{p}_i^+\right) \\ \dfrac{1}{R_g}\left(\bar{p}_i \bar{u}_i(\bar{\gamma}_i-1)\hat{p}_i^+ - \bar{p}_i \hat{u}_i^+\right) \\ \dfrac{1}{A_i}\left(\dfrac{\hat{u}_i^+}{\bar{u}_i}\right) \end{bmatrix}. \qquad (B9)$$

- **Area increase**. The components of the vector $\boldsymbol{P}$ are given by the fluctuating components of Eqs. (6a). Their corresponding adjoint variables are given by the numbers $\hat{\boldsymbol{a}}^+ = [a_m^+, a_x^+, a_e^+]^T$ respectively. The relationship between adjoint variables at the area increase and those defined in the ducts is given by: $\hat{\boldsymbol{a}}^+ = \hat{\boldsymbol{f}}_{\boldsymbol{2}}^+$. The adjoint jump conditions for an area increase are given by:

$$\hat{\boldsymbol{f}}_{\boldsymbol{1}}^+ = \hat{\boldsymbol{f}}_{\boldsymbol{2}}^+ + \hat{\phi}^+ \left[\left(\bar{h}_1 - \dfrac{\bar{u}_1^2}{2}\right)(\bar{\gamma}_1-1) - 2\bar{c}_1^2 \ , \ \dfrac{\bar{c}_1^2}{\bar{u}_1} + (\bar{\gamma}_1-1)\bar{u}_1 \ , \ -(\bar{\gamma}_1-1)\right]^T, \qquad (B10)$$

  where

$$\hat{\phi}^+ = \frac{A_2 - A_1}{A_1}\left(\frac{\bar{u}_1}{\bar{c}_1^2 - \bar{u}_1^2}\right)\hat{f}_{x_2}^+.$$

- **Area decrease**. The components of vector $\boldsymbol{P}$ are given by the fluctuating components of Eqs. (6b). Their corresponding adjoint variables are given by the numbers $\hat{\boldsymbol{b}}^+ = [b_m^+, b_s^+, b_e^+]^T$ respectively. The relationship between adjoint variables at the area decrease and those defined in the ducts is given by: $\hat{\boldsymbol{b}}^+ = \hat{\boldsymbol{s}}_{\boldsymbol{2}}^+$. The adjoint jump conditions for an area decrease are given by:

$$\hat{\boldsymbol{s}}_{\boldsymbol{1}}^+ = \hat{\boldsymbol{s}}_{\boldsymbol{2}}^+. \qquad (B11)$$

- **Heat source**. The components of vector $\boldsymbol{P}$ are given by the fluctuating components of Eqs. (6c). The corresponding adjoint variables are given by the numbers $\hat{\boldsymbol{c}}^+ = [c_m^+, c_x^+, c_e^+]^T$ respectively. The relationship between adjoint variables at the heat source and those defined in the ducts are given by: $\hat{\boldsymbol{c}}^+ = \hat{\boldsymbol{f}}_{\boldsymbol{2}}^+$. The adjoint jump conditions for a heat source are given by:

$$\hat{\boldsymbol{f}}_{\boldsymbol{1}}^+ = \hat{\boldsymbol{f}}_{\boldsymbol{2}}^+ - \hat{Q}^+ \left[\bar{h}_1(\gamma_1-1) - \bar{c}_1^2 - \dfrac{1}{2}\bar{u}_1^2(\gamma_1+1) \ , \ \gamma_1 \bar{u}_1 \ , \ -(\gamma_1-1)\right]^T. \qquad (B12)$$

  where

$$\hat{Q}^+ = \eta h_r \frac{\text{FTF}^*}{(\bar{c}_1^2 - \bar{u}_1^2)}\hat{f}_{e_2}^+, \qquad (B13)$$

To obtain the adjoint boundary conditions for the fluctuating flow, we begin by recasting the inlet and outlet boundary conditions Eqs. (8) and (9) in terms of fluctuating variables (instead of wave amplitudes):

$$\hat{p}\,(1 - R_c) + \bar{\rho}\bar{c}\hat{u}\,(1 + R_c) = 0, \tag{B14}$$

where $R_c = R_{ci}$ at the inlet and $R_c = R_{co}$ at the outlet.

- **Inlet boundary condition**. The component of vector $\boldsymbol{P}$ is given by Eq. (B14). The corresponding adjoint variable is b_i^+. The relationship between the adjoint variables at the boundary condition and those defined in the ducts is given by: $b_i^+ = 1/\left(\bar{\rho}\bar{c}(1 + R_{ci}^*)\right)\left(\bar{\rho}\hat{\rho}^+ + \bar{\rho}\bar{u}\hat{u}^+ + \bar{\gamma}\bar{p}\hat{p}^+\right)$. The adjoint inlet boundary condition is given by:

$$A_+^+ - \frac{1}{R_{ci}^*}\left(\frac{1 - \bar{M}}{1 + \bar{M}}\right) A_-^+ = 0, \tag{B15}$$

- **Outlet boundary condition**. The component of vector $\boldsymbol{P}$ is given by Eq. (B14). The corresponding adjoint variable is b_o^+. The relationship between the adjoint variables at the boundary condition and those defined in the ducts is given by: $b_o^+ = -1/\left(\bar{\rho}\bar{c}(1 + R_{co}^*)\right)\left(\bar{\rho}\hat{\rho}^+ + \bar{\rho}\bar{u}\hat{u}^+ + \bar{\gamma}\bar{p}\hat{p}^+\right)$. The adjoint outlet boundary condition is given by:

$$A_-^+\mathrm{e}^{ik_- L_t} - \frac{1}{R_{co}^*}\left(\frac{1 + \bar{M}}{1 - \bar{M}}\right) A_+^+\mathrm{e}^{ik_+ L_t} = 0. \tag{B16}$$

The adjoint problem evolves backwards in time. It is solved by shooting from the outlet towards the inlet in the network model. The adjoint eigenvalues are the complex conjugate of the direct eigenvalues. Hence, once we know a direct eigenvalue, we use its complex conjugate to shoot through the network and obtain the adjoint global mode $\{\omega^*; \hat{\rho}^+, \hat{u}^+, \hat{p}^+\}$, which is used to compute the optimality conditions.

Eigenvalue sensitivity analysis requires the direct and adjoint variables to be normalized. The normalization condition is obtained with the derivatives with respect to the eigenvalue of all of the frequency-dependent terms in the Lagrangian functional Eq. (B1). In its most general form it is given by:

$$i\left(\langle\hat{\rho}^+,\hat{\rho}\rangle + \langle\hat{u}^+,\bar{\rho}\hat{u}\rangle + \langle\hat{p}^+,\hat{p}\rangle\right) + \left\{\hat{c}_e^+, -\bar{Q}\frac{\partial\mathrm{FTF}}{\partial\omega}\frac{\hat{u}}{\bar{u}}\right\} + \left\{\hat{b}_o^+, \frac{\partial R_{co}}{\partial\omega}\left(-\hat{p} + \bar{\rho}\bar{c}\hat{u}\right)\right\} = 1. \tag{B17}$$

3.   Adjoint base flow equations

To derive the adjoint base flow equations we are interested in both inner products of Eq. (B1).

For a straight duct, the relevant components of vector $\boldsymbol{B}$ are given by Eqs. (2). The corresponding adjoint variables (components of vector $\boldsymbol{G}^+$) are given by the spatial functions $[R^+(x), U^+(x), P^+(x)]^T$ respectively. The

resulting adjoint base flow equations are given by:

$$\bar{u}\frac{\mathrm{d}R^+}{\mathrm{d}x} = \underbrace{-i\omega^*\hat{u}^*\hat{u}^+ + \left(\hat{\rho}^+ + \bar{u}\hat{u}^+ - \hat{p}^+\bar{p}\frac{\mathrm{d}\bar{\gamma}}{\mathrm{d}\bar{\rho}}\right)\frac{\mathrm{d}\hat{u}^*}{\mathrm{d}x}}_{\nabla_M}, \tag{B18a}$$

$$\bar{\rho}\frac{\mathrm{d}R^+}{\mathrm{d}x} + \bar{\rho}\bar{u}\frac{\mathrm{d}U^+}{\mathrm{d}x} + \gamma\bar{p}\frac{\mathrm{d}P^+}{\mathrm{d}x} = \underbrace{\hat{\rho}^+\frac{\mathrm{d}\hat{\rho}^*}{\mathrm{d}x} + \bar{\rho}\hat{u}^+\frac{\mathrm{d}\hat{u}^*}{\mathrm{d}x} + \hat{p}^+\frac{\mathrm{d}\hat{p}^*}{\mathrm{d}x}}_{\nabla_F}, \tag{B18b}$$

$$\frac{\mathrm{d}U^+}{\mathrm{d}x} + \bar{u}\frac{\mathrm{d}P^+}{\mathrm{d}x} = \underbrace{\left(\bar{\gamma} + \bar{p}\frac{\mathrm{d}\bar{\gamma}}{\mathrm{d}\bar{p}}\right)\hat{p}^+\frac{\mathrm{d}\hat{u}^*}{\mathrm{d}x}}_{\nabla_E}, \tag{B18c}$$

where $\mathrm{d}\bar{\gamma}/\mathrm{d}\bar{\rho} = -\mathrm{d}\bar{\gamma}/\mathrm{d}\bar{T}(\bar{p}/(\bar{\rho}^2 R_g))$ and $\mathrm{d}\bar{\gamma}/\mathrm{d}\bar{p} = \mathrm{d}\bar{\gamma}/\mathrm{d}\bar{T}(1/(\bar{\rho}R_g))$. The corresponding boundary terms are:

$$\left[\left(R^+\bar{u}\right)\delta\bar{\rho} + \left(R^+\bar{\rho} + U^+\bar{\rho}\bar{u} + P^+\gamma\bar{p}\right)\delta\bar{u} + \left(U^+ + \bar{u}P^+\right)\delta\bar{p}\right]_{x_0}^{x_1} = 0. \tag{B19}$$

As seen in Eqs. (B18), the adjoint base flow equations require knowledge of the adjoint perturbation variables. Hence, once the fluctuating adjoint problem is solved, we proceed to solve for the adjoint base flow equations, whose solutions are given by:

$$R^+(x) = R^+(x_1) - \int_x^{x_1} \frac{\nabla_M}{\bar{u}}\,\mathrm{d}x, \tag{B20a}$$

$$P^+(x) = P^+(x_1) - \int_x^{x_1} \frac{-\bar{\rho}\nabla_M + \bar{u}\nabla_F - \bar{\rho}\bar{u}^2\nabla_E}{\bar{\gamma}\bar{p}\bar{u} - \bar{\rho}\bar{u}^3}\,\mathrm{d}x, \tag{B20b}$$

$$U^+(x) = U^+(x_1) - \int_x^{x_1} \frac{\bar{\rho}\nabla_M - \bar{u}\nabla_F + \bar{\gamma}\bar{p}\nabla_E}{\bar{\gamma}\bar{p} - \bar{\rho}\bar{u}^2}\,\mathrm{d}x. \tag{B20c}$$

b. Jump conditions

For modules governed by mass, axial momentum and energy fluxes, we define the following adjoint base flow fluxes, which depend on the side i of the jump condition:

$$\boldsymbol{F_i^+} \equiv \begin{bmatrix} F_{m_i}^+ \\ F_{x_i}^+ \\ F_{e_i}^+ \end{bmatrix} = \begin{bmatrix} \frac{1}{A_i}\left(R_i^+ - \bar{u}_i U_i^+ + \left(\bar{c}_i^2 - \bar{h}_i(\bar{\gamma}_i - 1) + \frac{1}{2}(\bar{\gamma}_i - 1)\bar{u}_i^2\right)P_i^+\right) \\ \frac{1}{A_i}\left(U_i^+ - (\bar{\gamma}_i - 1)\bar{u}_i P_i^+\right) \\ \frac{1}{A_i}(\bar{\gamma}_i - 1)P_i^+ \end{bmatrix} + \begin{bmatrix} J_{M_i} \\ J_{X_i} \\ J_{E_i} \end{bmatrix} \tag{B21}$$

where $\boldsymbol{J_i} = [J_{M_i}, J_{X_i}, J_{E_i}]^T$ are functions of the fluctuating variables (direct and adjoint). They depend on the type of jump condition and are given by:

$$\boldsymbol{J_i} = \left(a_m^+ \mathrm{B}_{m_i} + a_x^+ \mathrm{B}_{x_i} + a_e^+ \mathrm{B}_{e_i}\right)[\hat{p}_i^*, \hat{\rho}_i^*, \hat{u}_i^*]^T, \tag{B22}$$

where a_m^+, a_x^+ and a_e^+ should be replaced according to the relevant jump condition and considering $\Gamma_i = \bar{\gamma}_i\bar{p}_i - \bar{\rho}_i\bar{u}_i^2$ and

$$\boldsymbol{f_c} = \left[\bar{h}_i(\bar{\gamma}_i - 1) - \bar{c}_i^2 - \frac{1}{2}\bar{u}_i^2(\bar{\gamma}_i + 1)\ ,\ \bar{\gamma}_i\bar{u}_i\ ,\ -(\bar{\gamma}_i - 1)\right]^T,$$

the B matrices are given by:

$$
\mathrm{B}_{m_i} = \frac{1}{\Gamma_i} \left[\; \mathbf{0} \; \middle| \; \boldsymbol{f_c} \; \middle| \; -\frac{\bar{\rho}_i}{\bar{u}_i} \left(\boldsymbol{f_c} + \begin{bmatrix} \bar{c}_i^2 - \bar{u}_i^2 \\ 0 \\ 0 \end{bmatrix} \right) \right],
\tag{B23}
$$

$$
\mathrm{B}_{x_i} = \frac{1}{\Gamma_i} \left[\; \mathbf{0} \; \middle| \; 2\bar{u}_i \boldsymbol{f_c} \; \middle| \; -2\bar{\rho}_i \begin{bmatrix} \bar{c}_i^2 - \bar{u}_i^2 \\ 0 \\ 0 \end{bmatrix} \right],
\tag{B24}
$$

$$
\mathrm{B}_{e_i} = \frac{1}{\Gamma_i} \left[\; \frac{\bar{\gamma}_i}{\bar{\gamma}_i - 1} \boldsymbol{f_c} \; \middle| \; \left(\bar{h}_i - \frac{\bar{c}_i^2}{\bar{\gamma}_i - 1} + \frac{3}{2}\bar{u}_i^2 \right) \boldsymbol{f_c} \; \middle| \; -\frac{\bar{\rho}_i}{\bar{u}_i} \left(\left(\bar{h}_i - \frac{\bar{u}_i^2}{2} \right) \boldsymbol{f_c} + (\bar{c}_i^2 - \bar{u}_i^2) \begin{bmatrix} \bar{u}_i^2 \\ 0 \\ 1 \end{bmatrix} \right) \right] \cdots
\tag{B25}
$$

$$
+ \frac{\Lambda}{\Gamma_i} \left[\; -\bar{M}_i^2 \boldsymbol{f_c} + (1 - \bar{M}_i^2) \begin{bmatrix} \bar{h}_i + \frac{\bar{u}_i^2}{2} \\ 0 \\ -1 \end{bmatrix} \; \middle| \; \frac{\bar{u}_i^2}{\bar{\gamma}_i} \boldsymbol{f_c} - \frac{\bar{c}_i^2 - \bar{u}_i^2}{\bar{\gamma}_i} \begin{bmatrix} \bar{h}_i + \frac{\bar{u}_i^2}{2} \\ 0 \\ -1 \end{bmatrix} \; \middle| \; \mathbf{0} \right],
$$

with

$$
\Lambda = \frac{\mathrm{d}c_p(\bar{T}_i)}{\mathrm{d}\bar{T}_i} \frac{(\bar{\gamma}_i - 1)\bar{T}_i}{R_g}.
$$

For modules governed by mass and energy fluxes together with entropy conservation we define the following adjoint base flow fluxes:

$$
\boldsymbol{S_i^+} \equiv \begin{bmatrix} S_{m_i}^+ \\ S_{s_i}^+ \\ S_{e_i}^+ \end{bmatrix} = \begin{bmatrix} \frac{1}{A_i} \left(R_i^+ - \left(\frac{1}{2}\bar{u}_i + \frac{\bar{h}_i}{\bar{u}_i} \right) U_i^+ + \bar{c}_i^2 P_i^+ \right) \\ \frac{1}{R_g} \left(\bar{p}_i \bar{u}_i (\bar{\gamma}_i - 1) P_i^+ - \bar{p}_i U_i^+ \right) \\ \frac{1}{A_i} \left(\frac{U_i^+}{\bar{u}_i} \right) \end{bmatrix} + \begin{bmatrix} K_{M_i} \\ K_{S_i} \\ K_{E_i} \end{bmatrix}.
\tag{B26}
$$

where $\boldsymbol{K_i} = [K_{M_i}, K_{S_i}, K_{E_i}]^T$ is given by:

$$
\boldsymbol{K_i} = \left(b_m^+ \mathrm{C}_{m_i} + b_s^+ \mathrm{C}_{s_i} + b_e^+ \mathrm{C}_{e_i} \right) [\hat{p}_i^*, \hat{\rho}_i^*, \hat{u}_i^*]^T.
\tag{B27}
$$

Again b_m^+, b_s^+ and b_e^+ should be replaced according to the relevant jump condition and considering $\beta_i = \bar{c}_i^2 - \bar{u}_i^2$ and

$$
\boldsymbol{g_c} = \frac{1}{\bar{\rho}_i} \left[-\left(\bar{h}_i + \frac{1}{2}\bar{u}_i^2 + \bar{c}_i^2 \right) \; , \; -\frac{\bar{m}_i \bar{c}_i^2}{R_g} \; , \; 1 \right]^T,
\tag{B28}
$$

the matrices C become:

$$
\mathrm{C}_{m_i} = \frac{1}{\beta_i} \left[\; \mathbf{0} \; \middle| \; \boldsymbol{g_c} \; \middle| \; -\frac{\bar{\rho}_i}{\bar{u}_i} \left(\boldsymbol{g_c} \right) - \frac{1}{\bar{u}_i} \begin{bmatrix} \bar{c}_i^2 - \bar{u}_i^2 \\ 0 \\ 0 \end{bmatrix} \right],
\tag{B29}
$$

$$
\mathrm{C}_{s_i} = \frac{\bar{c}_p(\bar{T}_i)}{\bar{m}_i \beta_i} \left[\; \frac{\bar{\gamma}_i}{\bar{c}_i^2} \boldsymbol{g_c} + \frac{1 - \bar{M}_i^2}{\bar{\rho}_i} \begin{bmatrix} \bar{\gamma}_i \\ \frac{\bar{m}_i(\bar{\gamma}_i - 1)}{R_g} \\ 0 \end{bmatrix} \; \middle| \; -\boldsymbol{g_c} - \frac{1}{\bar{\rho}_i} \begin{bmatrix} \bar{c}_i^2 - \bar{u}_i^2 \\ 0 \\ 0 \end{bmatrix} \; \middle| \; \mathbf{0} \right] \cdots
\tag{B30}
$$

$$
+ \frac{\frac{\mathrm{d}\bar{c}_p(\bar{T}_i)}{\mathrm{d}\bar{T}_i}}{\bar{m}_i \bar{c}_p(\bar{T}_i) \beta_i} \left[\; -\bar{\gamma}_i \left(\boldsymbol{g_c} + \frac{\bar{c}_i^2 - \bar{u}_i^2}{\bar{\rho}_i} \begin{bmatrix} \frac{1}{\bar{m}_i} \\ \frac{\bar{m}_i}{R_g} \\ 0 \end{bmatrix} \right) \; \middle| \; \bar{c}_i^2 \left(\boldsymbol{g_c} + \frac{\bar{c}_i^2 - \bar{u}_i^2}{\bar{\rho}_i} \begin{bmatrix} \frac{1}{\bar{m}_i} \\ \frac{\bar{m}_i}{R_g} \\ 0 \end{bmatrix} \right) \; \middle| \; \mathbf{0} \right],
$$

$$
\mathrm{C}_{e_i} = \frac{1}{\beta_i} \left[\; \frac{\bar{\gamma}_i}{\bar{\gamma}_i - 1} \boldsymbol{g_c} \; \middle| \; \left(\bar{h}_i - \frac{\bar{c}_i^2}{\bar{\gamma}_i - 1} + \frac{3}{2}\bar{u}_i^2 \right) \boldsymbol{g_c} \; \middle| \; -\frac{\bar{\rho}_i}{\bar{u}_i} \left(\bar{h}_i - \frac{\bar{u}_i^2}{2} \right) \boldsymbol{g_c} - \frac{1}{\bar{u}_i} (\bar{c}_i^2 - \bar{u}_i^2) \begin{bmatrix} \bar{u}_i^2 \\ 0 \\ 1 \end{bmatrix} \right] \cdots
\tag{B31}
$$

$$+ \frac{\Lambda}{\beta_i} \left[-\boldsymbol{g_c} - \frac{\bar{c}_i^2 - \bar{u}_i^2}{\bar{\rho}_i} \begin{bmatrix} \frac{1}{\bar{m}_i} \\ R_g \\ 0 \end{bmatrix} \middle| \frac{\bar{c}_i^2}{\bar{\gamma}_i} \left(\boldsymbol{g_c} + \frac{\bar{c}_i^2 - \bar{u}_i^2}{\bar{\rho}_i} \begin{bmatrix} \frac{1}{\bar{m}_i} \\ R_g \\ 0 \end{bmatrix} \right) \middle| \mathbf{0} \right].$$

- **Area increase**. The relevant components of vector $\boldsymbol{B}$ are given by the steady quantities of Eq. (6a). The corresponding adjoint variables are given by the numbers $\boldsymbol{A^+} = [A_m^+, A_x^+, A_e^+]^T$. The relationship between adjoint variables at the area increase and those defined at the duct is given by: $\boldsymbol{A^+} = \boldsymbol{F_2^+}$. The jump conditions are given by:

$$\boldsymbol{F_1^+} = \boldsymbol{F_2^+} + \Phi^+ \left[\left(\bar{h}_1 - \frac{\bar{u}_1^2}{2} \right)(\bar{\gamma}_1 - 1) - 2\bar{c}_1^2 \,,\, \frac{\bar{c}_1^2}{\bar{u}_1} + (\bar{\gamma}_1 - 1)\bar{u}_1 \,,\, -(\bar{\gamma}_1 - 1) \right]^T, \tag{B32}$$

where

$$\Phi^+ = \frac{A_2 - A_1}{A_1} \left(\frac{\bar{u}_1}{\bar{c}_1^2 - \bar{u}_1^2} \right) F_{x_2}^+.$$

- **Area decrease**. The relevant components of vector $\boldsymbol{B}$ are given by the steady quantities of Eq. (6b). The adjoint variables are given by the numbers $\boldsymbol{B^+} = [B_m^+, B_s^+, B_e^+]^T$. The relationship between adjoint variables at the area decrease and those defined at the duct is given by: $\boldsymbol{B^+} = \boldsymbol{S_2^+}$. The jump conditions are given by:

$$\boldsymbol{S_1^+} = \boldsymbol{S_2^+}. \tag{B33}$$

- **Heat source**. The components of vector $\boldsymbol{B}$ are given by the steady quantities of Eqs. (6c). The adjoint variables are given by the numbers $\boldsymbol{C^+} = [C_m^+, C_x^+, C_e^+]^T$. The relationship between adjoint variables at the heat source and those defined at the duct is given by: $\boldsymbol{C^+} = \boldsymbol{F_2^+}$. The jump conditions are given by:

$$\boldsymbol{F_1^+} = \boldsymbol{F_2^+} + \hat{Q}^+ \frac{\hat{u}_1^*}{\bar{u}_1} \left(1 - \frac{\bar{u}_1}{\text{FTF}^*} \frac{\partial \text{FTF}^*}{\partial \bar{u}_1} \right) \left[\bar{h}_1(\bar{\gamma}_1 - 1) - \bar{c}_1^2 - \frac{1}{2}\bar{u}_1^2(\bar{\gamma}_1 + 1) \,,\, \bar{\gamma}_1 \bar{u}_1 \,,\, -(\bar{\gamma}_1 - 1) \right]^T \cdots \tag{B34}$$

$$+ \left[\eta h_r \left(\text{FTF}^* \frac{\hat{u}_1^*}{\bar{u}_1} \hat{f}_{e_2}^+ + F_{e_2}^+ \right) \,,\, 0 \,,\, 0 \right]^T.$$

c. Boundary conditions

The adjoint base flow boundary conditions depend on the type of base flow properties fixed at the inlet or outlet of the configuration.

- **Inlet boundary condition**. At the inlet of the configuration the mean mass flow rate $\bar{m}$ and the mean temperature $\bar{T}$ are fixed. These are the components of vector $\boldsymbol{B}$ in Eq. (B1). Their corresponding adjoint variables are given by $B_{i_m}^+$ and $B_{i_T}^+$. The relationship with the adjoint variables defined in the ducts is given by:

$$B_{i_m}^+ = \frac{1}{A} \left(R^+ + \bar{u}U^+ + \bar{c}^2 P^+ \right), \qquad B_{i_T}^+ = \bar{\rho}R_g \left(U^+ + \bar{u}P^+ - b_i^+ \frac{\bar{c}}{2} \left(1 + \frac{\mathrm{d}\bar{\gamma}}{\mathrm{d}\bar{T}} \frac{\bar{T}}{\bar{\gamma}} \right) \hat{u}^* (1 + R_{ci}^*). \right) \tag{B35}$$

The corresponding inlet boundary condition is:

$$U^+ \left(\frac{\bar{p}}{\bar{\rho}} - \bar{u}^2 \right) + \bar{u}P^+ \left(\frac{\bar{p}}{\bar{\rho}} - \bar{c}^2 \right) - b_i^+ \bar{c}\hat{u}^* (1 + R_{ci}^*) = 0. \tag{B36}$$

- **Outlet boundary condition**. At the outlet the mean pressure $\bar{p}$ is fixed. This is the only component of vector $\boldsymbol{B}$ in Eq. (B1). The corresponding adjoint variable is given by $B_{o_p}^+$, and its relationship with the adjoint variables defined in the duct is given by:

$$B_{o_p}^+ = -U^+ - \bar{u}P^+ - b_o^+ \left(\frac{\partial R_{co}^*}{\partial \bar{p}} (\hat{p}^* + \bar{\rho}\bar{c}\hat{u}^*) + \hat{u}^*(1 + R_{co}^*) \frac{\bar{c}}{2} \left(1 + \frac{\mathrm{d}\bar{\gamma}}{\mathrm{d}\bar{T}} \frac{\bar{T}}{\bar{\gamma}} \right) \right). \tag{B37}$$

FIG. 18: A duct (highlighted in gray) with an area increase at the inlet and an area decrease at the outlet. The dotted lines represent other jumps or boundary conditions.

The outlet boundary condition is set by:

$$R^+ = -\frac{b_o^+}{\bar{u}}\left(\frac{\partial R_{co}^*}{\partial \bar{\rho}}\left(\hat{p}^* + \bar{\rho}\bar{c}\hat{u}^*\right) - \hat{u}^*(1 + R_{co}^*)\frac{\bar{c}}{2}\left(1 + \frac{\mathrm{d}\bar{\gamma}}{\mathrm{d}\bar{T}}\frac{\bar{T}}{\bar{\gamma}}\right)\right),\tag{B38a}$$

$$P^+ = P_0^+,\tag{B38b}$$

$$U^+ = \frac{1}{\bar{\rho}\bar{u}}\left(-\bar{\rho}R^+ - \bar{\gamma}\bar{p}P^+ - b_o^+\frac{\partial R_{co}^*}{\partial \bar{u}}\left(\hat{p}^* + \bar{\rho}\bar{c}\hat{u}^*\right)\right).\tag{B38c}$$

Here P_0^+ is used to denote the initial guess and eventually the formal solution of the adjoint base flow problem.

4.   Optimality conditions

The optimality conditions provide the derivatives of the eigenvalue with respect to the geometric parameters. They are obtained through the following steps:

1. Compute the direct global mode $\{\omega; \hat{\rho}, \hat{u}, \hat{p}\}$.

2. Compute the adjoint global mode $\{\omega^*; \hat{\rho}^+, \hat{u}^+, \hat{p}^+\}$.

3. Solve the adjoint base flow problem to obtain P^+, R^+, U^+.

4. Normalize using Eq. (B17).

5. Obtain the first variation of the Lagrangian with respect to the parameter of interest.

The geometric parameters such as areas, lengths and mean radii enter the Lagrangian of a complex network non-trivially. Therefore we briefly discuss how to compute the sensitivities for each of them.

a.   Area

A change in area induces variations in the perturbation equations ($\boldsymbol{P}$) and in the base flow equations ($\boldsymbol{B}$). Therefore, we consider the contributions of each of them separately and then add them together. An area variation affects the jump conditions at the duct inlet and at the outlet (See Fig. 18). Thus setting the derivative of the Lagrangian with respect to the area to zero gives:

$$\frac{\partial \mathcal{L}}{\partial A}\delta A = 0 \implies \frac{\delta\omega}{\delta A} = \left(\frac{\delta\omega}{\delta A}\bigg|_{\boldsymbol{P}} + \frac{\delta\omega}{\delta A}\bigg|_{\boldsymbol{B}}\right)_{inlet} + \left(\frac{\delta\omega}{\delta A}\bigg|_{\boldsymbol{P}} + \frac{\delta\omega}{\delta A}\bigg|_{\boldsymbol{B}}\right)_{outlet}.\tag{B39}$$

For the duct highlighted in Fig. 18, we consider that the flow variables at the duct inlet are given by subscript 1 and the variables just before the duct inlet are given by subscript 0. The area sensitivities at the duct inlet are given by:

$$\left(\frac{\delta\omega}{\delta A}\bigg|_{\boldsymbol{P}}\right)_{inlet} = -\left\{\hat{a}_m^+, \bar{\rho}_1\hat{u}_1 + \hat{\rho}_1\bar{u}_1\right\} - \left\{\hat{a}_x^+, \hat{p}_1 + \hat{\rho}_1\bar{u}_1^2 + 2\bar{\rho}_1\bar{u}_1\hat{u}_1 - \hat{p}_0\right\}\cdots$$

$$-\left\{\hat{a}_e^+, \frac{\bar{\gamma}_1 \bar{u}_1}{\bar{\gamma}_1 - 1}\hat{p}_1 + \bar{\rho}_1\left(\bar{h}_1 + \frac{3}{2}\bar{u}_1^2\right)\hat{u}_1 + \bar{u}_1\left(\bar{h}_1 - \frac{\bar{c}_1^2}{(\bar{\gamma}_1 - 1)} + \frac{\bar{u}_1^2}{2}\right)\hat{\rho}_1\right\},$$

$$\left(\left.\frac{\delta\omega}{\delta A}\right|_{\boldsymbol{B}}\right)_{inlet} = -\left\{A_m^+, \bar{\rho}_1\bar{u}_1\right\} - \left\{A_x^+, \bar{p}_1 + \bar{\rho}_1\bar{u}_1^2 - \bar{p}_0\right\} - \left\{A_e^+, \bar{\rho}_1\bar{u}_1\left(\bar{h}_1 + \frac{1}{2}\bar{u}_1^2\right)\right\}.$$

We consider that the flow variables at the duct outlet are given by subscript 2 and the variables just after the duct outlet are given by subscript 3. The area sensitivities at the duct outlet are given by:

$$\left(\left.\frac{\delta\omega}{\delta A}\right|_{\boldsymbol{P}}\right)_{outlet} = -\left\{\hat{b}_m^+, -(\bar{\rho}_2\hat{u}_2 + \hat{\rho}_2\bar{u}_2)\right\}\cdots$$

$$-\left\{\hat{b}_e^+, -\left(\frac{\bar{\gamma}_2\bar{u}_2}{\bar{\gamma}_2 - 1}\hat{p}_2 + \bar{\rho}_2\left(\bar{h}_2 + \frac{3}{2}\bar{u}_2^2\right)\hat{u}_2 + \bar{u}_2\left(\bar{h}_2 - \frac{\bar{c}_2^2}{(\bar{\gamma}_2 - 1)} + \frac{\bar{u}_2^2}{2}\right)\hat{\rho}_2\right)\right\},$$

$$\left(\left.\frac{\delta\omega}{\delta A}\right|_{\boldsymbol{B}}\right)_{outlet} = -\left\{B_m^+, -(\bar{\rho}_2\bar{u}_2)\right\} - \left\{B_e^+, -\left(\bar{\rho}_2\bar{u}_2\left(\bar{h}_2 + \frac{1}{2}\bar{u}_2^2\right)\right)\right\}.$$

b. Length

In a given network model, the axial position of a jump condition or boundary condition is determined by the sum of the ducts' length that appear before that jump or boundary i.e., $x = L_1 + L_2 + \cdots + L_n$. To compute the local value of the perturbation variables at those locations, the axial position is required. Hence, to compute the sensitivity to a variation in a duct's length, we need to include all of the perturbation variables that used that length to compute its local value. Thus, setting the derivative of the Lagrangian with respect to the length to zero gives:

$$\frac{\partial\mathcal{L}}{\partial L}\delta L = 0 \implies \frac{\delta\omega}{\delta L} = \sum_{i=1}^{N}\frac{\delta\omega}{\delta L_i} \tag{B40}$$

where N is the number of jump conditions that appear after the desired duct length plus one that represents the outlet boundary condition, and $\delta\omega/\delta L_i$ represents the sensitivity of the length at a single location.

For example, consider that position 4 in Fig. 18 represents the acoustic reflection coefficient boundary condition. Let the subscript $_L$ represent a derivative of a perturbation variable or a perturbation flux with respect to L, i.e.,

$$\hat{p}_L = \frac{\partial\hat{p}}{\partial L} = A_+ik_+\mathrm{e}^{ik_+x} + A_-ik_-\mathrm{e}^{ik_-x}.$$

Then the sensitivity of the eigenvalue to variations of the highlighted duct's length is given by:

$$\frac{\partial\omega}{\partial L} = \frac{\delta\omega}{\delta L_j} + \frac{\delta\omega}{\delta L_b}$$

where

$$\frac{\delta\omega}{\delta L_j} = -\left\{\hat{b}_m^+, \hat{m}_{L_3} - \hat{m}_{L_2}\right\} - \left\{\hat{b}_s^+, \hat{s}_{L_3} - \hat{s}_{L_2}\right\} - \left\{\hat{b}_e^+, \hat{e}_{L_3} - \hat{e}_{L_2}\right\},$$

$$\frac{\delta\omega}{\delta L_b} = -\left\{\hat{b}_o^+, \hat{p}_{L_4}(1 - R_{co}) + \bar{\rho}\bar{c}\hat{u}_{L_4}(1 + R_{co})\right\}.$$

c. Mean radius

For this configuration the sensitivities of the mean radius are only relevant at two locations: the outlet duct and the ducts whose mean radius influence the FTF. For the outlet duct the sensitivity is given by

$$\frac{\delta\omega}{\delta R} = -\left\{b_o^+, \frac{\partial R_{co}}{\partial R}(-\hat{p} + \bar{\rho}\bar{c}\hat{u})\right\}, \tag{B41}$$

recalling that the radius in Eq. (10) is given by $r = A/(2\pi R)$. For the mean radii affecting the FTF, letting R_i, $i = 1, 2$ be the mean radius of the two relevant ducts, their sensitivities are given by:

$$\frac{\delta\omega}{\delta R_i} = -\left\{c_e^+, \frac{\partial\mathrm{FTF}}{\partial R_i}\frac{\hat{u}}{\bar{u}}\right\}. \tag{B42}$$

Appendix C: Fraction of disturbance energy retained in a cycle

In this appendix we show that the fraction of disturbance energy retained over a cycle is:

$$\check{E} \equiv \int_V E(t_0 + \mathcal{T}) \; \mathrm{d}V \Big/ \int_V E(t_0) \; \mathrm{d}V = \mathrm{e}^{2\lambda/f}. \tag{C1}$$

We begin with the disturbance energy density defined in Eq. (15):

$$E(t) = \frac{1}{2} \frac{p'^2}{\bar{\rho}\bar{c}^2} + \frac{1}{2}\bar{\rho}u'^2 + \rho'\bar{u}u' + \frac{1}{2}\frac{\bar{\rho}\bar{T}s'^2}{\bar{c}_p}, \tag{C2}$$

Which can be recast as

$$E(t) = \mathbf{q}^T \mathbf{M} \mathbf{q}, \tag{C3}$$

where $\mathbf{q}^T = [p', u', \rho', s']$. Recall that $p'(x,t) = \mathrm{Re}\{\hat{p}(x)\mathrm{e}^{i\omega t}\}$ such that $\mathbf{q} = \mathrm{Re}\{\hat{\mathbf{q}}(x)\mathrm{e}^{i\omega t}\}$. Then

$$\frac{\int_V E(t_0 + \mathcal{T}) \; \mathrm{d}V}{\int_V E(t_0) \; \mathrm{d}V} = \frac{\int_V \mathrm{Re}\{\hat{\mathbf{q}}(x)^T \mathrm{e}^{i\omega(t_0 + \mathcal{T})}\} \; \mathbf{M} \; \mathrm{Re}\{\hat{\mathbf{q}}(x)\mathrm{e}^{i\omega(t_0 + \mathcal{T})}\} \; \mathrm{d}V}{\int_V \mathrm{Re}\{\hat{\mathbf{q}}(x)^T \mathrm{e}^{i\omega t_0}\} \; \mathbf{M} \; \mathrm{Re}\{\hat{\mathbf{q}}(x)\mathrm{e}^{i\omega t_0}\} \; \mathrm{d}V} \tag{C4}$$

Using the definitions $\omega = 2\pi f - i\lambda$ and $\mathcal{T} = 1/f$:

$$\mathrm{e}^{i\omega(t_0 + \mathcal{T})} = \mathrm{e}^{i\omega(t_0)}\mathrm{e}^{i(2\pi f - i\lambda)/f} = \mathrm{e}^{i\omega(t_0)}\mathrm{e}^{\lambda/f}. \tag{C5}$$

The term $\mathrm{e}^{i\omega(\mathcal{T})} = \mathrm{e}^{\lambda/f}$ is real and independent of the volume, therefore:

$$\frac{\int_V E(t_0 + \mathcal{T}) \; \mathrm{d}V}{\int_V E(t_0) \; \mathrm{d}V} = \frac{\int_V \mathrm{Re}\{\hat{\mathbf{q}}(x)^T \mathrm{e}^{i\omega t_0}\}\mathrm{e}^{\lambda/f} \; \mathbf{M} \; \mathrm{Re}\{\hat{\mathbf{q}}(x)\mathrm{e}^{i\omega t_0}\}\mathrm{e}^{\lambda/f} \; \mathrm{d}V}{\int_V \mathrm{Re}\{\hat{\mathbf{q}}(x)^T \mathrm{e}^{i\omega t_0}\} \; \mathbf{M} \; \mathrm{Re}\{\hat{\mathbf{q}}(x)\mathrm{e}^{i\omega t_0}\} \; \mathrm{d}V} = \mathrm{e}^{2\lambda/f}. \tag{C6}$$

---

[1] T. C. Lieuwen and V. Yang, eds., *Combustion instabilities in gas turbine engines: operational experience, fundamental mechanisms, and modeling* (AIAA, 2005).

[2] D. Zhao and X. Li, A review of acoustic dampers applied to combustion chambers in aerospace industry, Progress in Aerospace Sciences **74**, 114 (2015).

[3] D. Zhao and A. S. Morgans, Tuned passive control of combustion instabilities using multiple Helmholtz resonators, Journal of Sound and Vibration **320**, 744 (2009).

[4] M. R. Bothien, N. Noiray, and B. Schuermans, A Novel Damping Device for Broadband Attenuation of Low-Frequency Combustion Pulsations in Gas Turbines, Journal of Engineering for Gas Turbines and Power **136**, 041504 (2013).

[5] A. P. Dowling and A. S. Morgans, Feedback control of combustion oscillations, Annual Review of Fluid Mechanics **37**, 151 (2005).

[6] Y. Huang and V. Yang, Dynamics and stability of lean-premixed swirl-stabilized combustion, Progress in Energy and Combustion Science **35**, 293 (2009).

[7] D. Zhao, Z. Lu, H. Zhao, X. Y. Li, B. Wang, and P. Liu, A review of active control approaches in stabilizing combustion systems in aerospace industry, Progress in Aerospace Sciences **97**, 35 (2018).

[8] M. P. Juniper and R. I. Sujith, Sensitivity and Nonlinearity of Thermoacoustic Oscillations, Annual Review of Fluid Mechanics **50**, 661 (2018), arXiv:1507.05135.

[9] L. Magri and M. P. Juniper, Sensitivity analysis of a time-delayed thermo-acoustic system via an adjoint-based approach, Journal of Fluid Mechanics **719**, 183 (2013).

[10] J. G. Aguilar, L. Magri, and M. P. Juniper, Adjoint-based sensitivity analysis of low-order thermoacoustic networks using a wave-based approach, Journal of Computational Physics **341**, 163 (2017), arXiv:arXiv:1508.04886v1.

[11] M. P. Juniper, Sensitivity analysis of thermoacoustic instability with adjoint Helmholtz solvers, Physical Review Fluids **3**, 10.1103/PhysRevFluids.3.110509 (2018).

[12] L. Magri, Adjoint Methods as Design Tools in Thermoacoustics, Applied Mechanics Reviews **71**, 020801 (2019).

[13] P. Luchini and A. Bottaro, Adjoint Equations in Stability Analysis, Annual Review of Fluid Mechanics **46**, 493 (2014).

[14] G. Rigas, N. P. Jamieson, L. K. B. Li, and M. P. Juniper, Experimental sensitivity analysis and control of thermoacoustic systems, Journal of Fluid Mechanics **787**, R1 1 (2016).

[15] N. P. Jamieson, G. Rigas, and M. P. Juniper, Experimental sensitivity analysis via a secondary heat source in an oscillating thermoacoustic system, International Journal of Spray and Combustion Dynamics **0**, 1 (2017).

[16] F. Caeiro, C. Sovardi, K. Förner, and W. Polifke, Shape optimization of a Helmholtz resonator using an adjoint method, International Journal of Spray and Combustion Dynamics **9**, 394 (2017).

[17] G. A. Mensah and J. P. Moeck, Acoustic Damper Placement and Tuning for Annular Combustors: An Adjoint-Based Optimization Study, Journal of Engineering for Gas Turbines and Power **139**, 061501 (2017).

[18] D. Yang, F. M. Sogaro, A. S. Morgans, and P. J. Schmid, Optimising the acoustic damping of multiple Helmholtz resonators attached to a thin annular duct, Journal of Sound and Vibration **444**, 69 (2019).

[19] O. Marquet, D. Sipp, and L. Jacquin, Sensitivity analysis and passive control of cylinder flow, Journal of Fluid Mechanics **615**, 221 (2008).

[20] A. P. Dowling and S. R. Stow, Acoustic analysis of gas turbine combustors, Journal of Propulsion and Power **19**, 751 (2003).

[21] S. R. Stow and A. P. Dowling, A Time-Domain Network Model for Nonlinear Thermoacoustic Oscillations, Journal of Engineering for Gas Turbines and Power **131**, 031502 (2009).

[22] J. Li, Y. Xia, A. S. Morgans, and X. Han, Numerical prediction of combustion instability limit cycle oscillations for a combustor with a long flame, Combustion and Flame **185**, 28 (2017).

[23] V. Bellucci, B. Schuermans, D. Nowak, P. Flohr, and C. O. Paschereit, Thermoacoustic Modeling of a Gas Turbine Combustor Equipped With Acoustic Dampers, Journal of Turbomachinery **127**, 372 (2005).

[24] T. C. Lieuwen, *Unsteady Combustor Physics*, 1st ed. (2012).

[25] M. R. Bothien, *Impedance Tuning : A Method for Active Control of the Acoustic Boundary Conditions of Combustion Test Rigs*, Ph.D. thesis, Technische Universität Berlin (2008).

[26] S. R. Stow and A. P. Dowling, Thermoacoustic oscillations in an annular combustor, ASME Turbo Expo , 2001 (2001).

[27] S. R. Stow and A. P. Dowling, Modelling of Circumferential Modal Coupling due to Helmholtz resonators, ASME Turbo Expo (2003).

[28] S. R. Stow and A. P. Dowling, Low-order modelling of thermoacoustic limit cycles, ASME Turbo Expo (2004).

[29] J. G. Aguilar, *Sensitivity analysis and optimization in low order thermoacoustic models*, Ph.D. thesis, University of Cambridge (2018).

[30] J. Li and A. S. Morgans, Simplified models for the thermodynamic properties along a combustor and their effect on thermoacoustic instability prediction, Fuel **184**, 735 (2016).

[31] R. Balachandran, *Experimental Investigation of the Response of Turbulent Premixed Flames to Acoustic Oscillations*, Ph.D. thesis, University of Cambridge (2005).

[32] B. J. McBride, M. J. Zehe, and S. Gordon, NASA Glenn Coefficients for Calculating Thermodynamic Properties of Individual Species, Technical report NASA **211556**, 291 (2002).

[33] X. Han, J. Li, and A. S. Morgans, Prediction of combustion instability limit cycle oscillations by combining flame describing function simulations with a thermoacoustic network model, Combustion and Flame **162**, 3632 (2015).

[34] H. Levine and J. Schwinger, On the radiation of sound from an unflanged circular pipe, Physical Review **73**, 383 (1948).

[35] A. M. Cargill, Low frequency acoustic radiation from a jet pipe - a second order theory, Journal of Sound and Vibration **83**, 339 (1982).

[36] M. C. a. M. Peters, a. Hirschberg, a. J. Reijnen, and a. P. J. Wijnands, Damping and reflection coefficient measurements for an open pipe at low Mach and low Helmholtz numbers, Journal of Fluid Mechanics **256**, 499 (1993).

[37] M. Gunzburger, Inverse design and optimisation methods. Introduction into mathematical aspects of flow control and optimization, in *von Karman Institute for Fluid Dynamics, Lecture Series 1997-05* (1997).

[38] W. Press, S. Teukolsky, W. Vetterling, B. Flannery, E. Ziegel, W. Press, B. Flannery, S. Teukolsky, and W. Vetterling, *Numerical Recipes: The Art of Scientific Computing*, 2nd ed. (Cambridge University Press, Cambridge, 1992).

[39] M. K. Myers, Transport of energy by disturbances in arbitrary steady flows, Journal of Fluid Mechanics **226**, 383 (1991).

[40] N. Karimi, M. J. Brear, and W. H. Moase, Acoustic and disturbance energy analysis of a flow with heat communication, Journal of Fluid Mechanics **597**, 67 (2008).

[41] M. J. Brear, F. Nicoud, M. Talei, A. Giauque, and E. R. Hawkes, Disturbance energy transport and sound production in gaseous combustion, Journal of Fluid Mechanics **707**, 53 (2012).

[42] L. Magri, M. Bauerheim, F. Nicoud, and M. P. Juniper, Stability analysis of thermo-acoustic nonlinear eigenproblems in annular combustors. Part II. Uncertainty quantification, Journal of Computational Physics **325**, 411 (2016).

[43] Xiaochuan Yuan, K. Glover, and A. P. Dowling, Modeling investigation for thermoacoustic oscillation control, in *Proceedings of the 2010 American Control Conference* (IEEE, 2010) pp. 3323–3328.

[44] A. N. Lipatnikov and J. Chomiak, Turbulent flame speed and thickness: Phenomenology, evaluation, and application in multi-dimensional simulations, Progress in Energy and Combustion Science **28**, 1 (2002).

[45] O. S. Graham, *Modelling the thermoacoustic response of premixed flames*, Ph.D. thesis, University of Cambridge (2012).

[46] B. Semlitsch, A. Orchini, A. P. Dowling, and M. P. Juniper, G-equation modelling of thermoacoustic oscillations of partially premixed flames, International Journal of Spray and Combustion Dynamics **9**, 260 (2017).

[47] D. H. Shin and T. Lieuwen, Flame wrinkle destruction processes in harmonically forced, turbulent premixed flames, Journal of Fluid Mechanics **721**, 484 (2013).